Check for updates

ADVANCING EARTH AND SPACE SCIENCES

JGR Machine Learning and Computation

RESEARCH ARTICLE
10.1029/2025JH000965

Reconstructing Magnetotail Reconnection Events Using Data Mining is Feasible and Repeatable

G. K. Stephens[1], **R. S. Weigel**[2], **M. I. Sitnov**[1], **and N. A. Tsyganenko**[3]

[1]The Johns Hopkins University Applied Physics Laboratory, Laurel, MD, USA, [2]George Mason University, Fairfax, VA, USA, [3]Saint-Petersburg State University, Saint-Petersburg, Russia

Abstract Recently, Stephens et al. (2023), https://doi.org/10.1029/2022ja031066 utilized a data mining (DM) algorithm, applied to 26 years of magnetospheric magnetometer observations coupled with a flexible formulation of the magnetospheric magnetic field, to reconstruct the global configuration of the magnetotail when the Magnetospheric MultiScale (MMS) mission observed tail reconnection in situ. Of the 26 DM-reconstructed MMS reconnection events, 16 had a $B_z = 0$ isocontour within ≈ 2 Earth radii (R_E) of the observed reconnection location. Another eight had a B_z minimum region, identified using $B_z = 2$ nT isocontours, within $\approx 2R_E$. This consistency suggests that the structure of tail reconnection is correlated with the substorm/storm state of the magnetosphere, as reflected by geomagnetic indices and solar wind conditions. We verify these results using new validation methods and by comparing in-sample (including event data) to out-of-sample (excluding event data) reconstructions. We first benchmark the architecture of the reconstructed magnetic field using 100 randomly generated magnetic fields containing tail X- and O-lines, resolving 77 of them with three false positives. Next, we quantify the consistency of the reconstructions in resolving the reconnection location using a skill score relative to random chance. 88% of the in-sample and 75% of the out-of-sample scores are positive, confirming that the reconstructions resolve the location of tail reconnection better than random chance. Last, a bootstrapping analysis, which refits the model architecture to 100 random resamples of data, shows standard deviations in B_z of $\lesssim 1$ nT, indicating that the DM approach is not overly sensitive to the particular sampling of magnetometer records.

Plain Language Summary The Earth's magnetotail is a region on the nightside of Earth where the interaction between the Earth's intrinsic magnetic field and the solar wind stretches the field. Magnetic reconnection occurs within the electric current sheet at the center of the stretched magnetic field, leading to a reconfiguration of the magnetotail and the energization of charged particles. Tail reconnection is a crucial process in large-scale space weather events, including geomagnetic storms and substorms. Knowing where and when tail reconnection occurs during these events is necessary to understand how they work. A spacecraft can observe tail reconnection when it flies through the region where it occurs, as the Magnetospheric MultiScale (MMS) mission has done, finding at least 26 tail reconnection events. The magnetic field configuration for these events was reconstructed using a data mining-based algorithm that searches through decades of space magnetic field observations for data when the tail was in a comparable storm and substorm state. The identified data constrain a mathematical model representing the tail magnetic field. A previous study showed that the reconstructed magnetic field was generally consistent with the observed reconnection locations. This study further supports the prior one by using more advanced methods.

Key Points:

- The magnetic field architecture used in data mining reconstructions of tail reconnection events is capable of resolving most X- and O-lines
- Both in-sample and out-of-sample reconstructions possess skill in identifying the location of tail reconnection over random chance
- A bootstrapping analysis indicates that the reconstructions are not overly sensitive to the particular sample of magnetometer records

Supporting Information:

Supporting Information may be found in the online version of this article.

Correspondence to:

G. K. Stephens,
Grant.Stephens@jhuapl.edu

Citation:

Stephens, G. K., Weigel, R. S., Sitnov, M. I., & Tsyganenko, N. A. (2026). Reconstructing magnetotail reconnection events using data mining is feasible and repeatable. *Journal of Geophysical Research: Machine Learning and Computation*, *3*, e2025JH000965. https://doi.org/10.1029/2025JH000965

Received 10 SEP 2025
Accepted 19 DEC 2025

Author Contributions:

Conceptualization: G. K. Stephens, R. S. Weigel
Data curation: G. K. Stephens
Formal analysis: G. K. Stephens
Funding acquisition: G. K. Stephens, M. I. Sitnov
Investigation: G. K. Stephens
Methodology: G. K. Stephens, R. S. Weigel, M. I. Sitnov, N. A. Tsyganenko
Project administration: G. K. Stephens

1. Introduction

Magnetic reconnection is a fundamental process of space plasmas that converts energy stored in the magnetic field into particle kinetic and thermal energy (Hesse & Cassak, 2020). In the Earth's magnetosphere, reconnection readily occurs at the dayside magnetopause when the interplanetary magnetic field (IMF), carried by the solar wind, contains a southward component, $B_z^{\mathrm{IMF}} < 0$ (e.g., Newell et al., 2007, and refs. therein). Dayside reconnection connects the Earth's magnetic field to the IMF, initiating the Dungey cycle (Dungey, 1961). Dayside reconnection is relatively well understood from first principles (Borovsky, 2008; Cassak & Shay, 2007) and its location can be modeled empirically (Trattner et al., 2007, 2012, 2021). In contrast to dayside reconnection, magnetotail reconnection is often explosive in nature (Sitnov, Birn, et al., 2019) and its location is relatively unknown (e.g., McPherron, 2016) due to the rarity and sparsity of *in situ* observations within its vast volume. Knowing the location of tail reconnection is crucial to understanding the global dynamics of the magnetosphere

Resources: G. K. Stephens, M. I. Sitnov
Software: G. K. Stephens, N. A. Tsyganenko
Supervision: R. S. Weigel
Validation: G. K. Stephens
Visualization: G. K. Stephens
Writing – original draft: G. K. Stephens
Writing – review & editing: G. K. Stephens, R. S. Weigel, M. I. Sitnov, N. A. Tsyganenko

during active times, as it drives key space weather phenomena such as magnetospheric substorms (Baker et al., 1996; Hones Jr, 1979; Hones Jr, 1984; McPherron, Russell, & Aubry, 1973) and geomagnetic storms (Angelopoulos et al., 2020; Miyashita et al., 2005; Sciola et al., 2023). The location and evolution of magnetotail reconnection, along with the global structure of the surrounding magnetic field, have implications for the kinetic physics describing substorm onset (Sitnov, Birn, et al., 2019). The radial location also determines the magnitude of the reconnecting magnetic field and thereby how much energy is available for particle heating (Angelopoulos et al., 2020). The local time position of reconnection in the tail correlates with the location of the substorm current wedge and thus also with its ionospheric and ground manifestations (Nagai & Shinohara, 2021). Further, if the location of reconnection is known, particularly for a specific event, this information can guide first-principles models. For instance, tail reconnection can be initiated in the observed location during global magnetohydrodynamic simulations by placing a region of finite resistivity into the Ohm's law equation, thereby enabling event-specific substorm simulations (Arnold et al., 2023).

Magnetotail reconnection can be observed in situ when a spacecraft travels through where charged particles are demagnetized, termed the diffusion region (DR). Due to the smaller gyroradii of electrons relative to ions, the smaller electron DR (EDR) is embedded within the larger ion DR (IDR) (Shay et al., 1998), thereby making fortuitous spacecraft encounters of the IDR more likely. The magnetic field topology within the DR resembles the letter "X" when viewed from the x-z plane (in the Geocentric Solar Magnetospheric or GSM system), which extends roughly along the y direction, forming an X-line. Earthward of the X-line, the magnetic field possesses a northward component $\left(B_z > 0\right)$ and the bulk reconnection plasma outflows stream toward the Earth ($v_{x,\text{out}} > 0$), while tailward of the X-line these are reversed ($B_z < 0$ and $v_{x,\text{out}} < 0$). Along the X-line itself, the z-component of the magnetic field should be at or near zero $\left(B_z \approx 0\right)$. Therefore, a spacecraft traversing across a diffusion region will observe a correlated reversal in the z-component of the magnetic field and the x-component of the plasma bulk velocity (Ueno et al., 1999). An additional observational signature of reconnection within the DR region is the presence of Hall electric and magnetic fields (Eastwood et al., 2007). Tailward of the X-line is a second magnetic neutral line termed the O-line, reflecting the magnetic topology where the field lines now encircle the neutral line (Dungey, 1953; Fukao et al., 1975; McPherron, Russell, Kivelson, & Coleman, 1973; Stern, 1979).

A method for elucidating information on the statistical location of tail reconnection is to perform systematic surveys searching for the aforementioned reconnection signatures. Using this approach, Eastwood et al. (2010) identified 18 tail reconnection sites using Cluster data. Several similar surveys have been conducted using the Geotail mission, the most recent being Nagai et al. (2023), which identified 243 tail reconnection events. Using this large set of reconnection events, the authors concluded that tail reconnection primarily occurred between $-30 \le x \le -23 R_E$, although intense solar wind driving, characterized by periods with significant negative vB_z^{IMF} where v is the opposite of the x-component of the solar wind velocity, shifted the reconnection site closer to Earth. Under nominal conditions, tail reconnection is more frequently observed in the pre-midnight (dusk) sector and shifts dawnward/duskward during intense/weak driving. These findings largely confirmed and refined earlier Geotail investigations, which used a smaller number of events (Nagai et al., 1998, 2005; Nagai & Shinohara, 2021). Using a combined reconnection event list from the Geotail and Cluster missions, Genestreti et al. (2013, 2014) developed an empirical occurrence rate model for tail reconnection as a function of the x and y position. They found a relatively constant occurrence rate as a function of x from -15 to $-30 R_E$ with a clear bias in the y position toward dusk. A similar survey was later conducted using data from the Magnetospheric MultiScale (MMS) mission, identifying 26 IDR events (Rogers et al., 2019, 2023).

Stephens et al. (2023) reconstructed the magnetotail magnetic field during these 26 IDR events, labeled events A–Z, using a data mining (DM) based empirical reconstruction algorithm, termed SST19 (Sitnov, Stephens, et al., 2019; Stephens et al., 2019). SST19 resolves the magnetospheric magnetic field using an analytical formulation that models the primary magnetospheric current systems in a manner similar to classical Tsyganenko-style empirical magnetic field models (Tsyganenko, 2013; Tsyganenko, Andreeva, Kubyshkina, et al., 2021). However, in contrast to these earlier "modular" empirical magnetic field models, SST19, along with its predecessor TS07D (Sitnov et al., 2008; Tsyganenko & Sitnov, 2007), represents the equatorial current systems using flexible expansions and utilizes a DM algorithm to capture the temporal evolution of the magnetosphere. Such flexible approaches, with a large number ($\sim 10^2$–10^3) of degrees of freedom, were made possible by the ever-increasing quantity of magnetospheric space missions along with nearly continuous monitoring of the solar wind by L1 spacecraft since the mid-1990s. The DM algorithm is based on the k-nearest neighbor (kNN) classifier method (Wettschereck et al., 1997). The global storm/substorm state of the magnetosphere is characterized by a low-dimensional state space (Vassiliadis, 2006), composed of both storm and substorm geomagnetic indices, their time derivatives, and the strength of the solar wind driving (Stephens et al., 2019). This approach was first applied to storm reconstructions (Sitnov et al., 2008; Sitnov & Schindler, 2010; Stephens et al., 2016) and was later tailored to substorms (Shi et al., 2024; Sitnov, Stephens, et al., 2019; Stephens et al., 2019; Stephens & Sitnov, 2021). The feasibility of this DM-based empirical picture of substorms was subsequently confirmed using a similar methodology that likewise employed the kNN method, albeit with a different storm/substorm state space and a different model architecture based on cylindrical basis functions (Tsyganenko, Andreeva, Sitnov, et al., 2021). Earlier SST19 empirical reconstructions of substorms identified potential tail reconnection regions (Sitnov et al., 2021; Sitnov, Stephens, et al., 2019; Turner et al., 2021), characterized when the reconstructed magnetic field had a zero z-component $\left(B_z = 0\right)$ within the neutral sheet. However, it was not evident at the time whether the reconstructed reconnection regions matched their true locations during these events. Stephens et al. (2023) addressed this by reconstructing the 26 MMS observed IDR events (Rogers et al., 2019, 2023) using SST19 and comparing the observed location of reconnection to the reconstructed z-component of the magnetic field within the neutral sheet. Of the 26 IDR event reconstructions, 16 resulted in $B_z = 0$ isocontours that were $<2R_E$ of where MMS observed an IDR. Another eight IDR reconstructions were instead near $\left(\lessapprox 2R_E\right)$ a B_z minimum region, defined by $B_z = 2$ nT isocontours. Thereby, 24 of the 26 IDR event reconstructions were consistent with the observed IDR location. However, there were issues regarding the generalizability of these findings, particularly since the SST19 reconstructions utilized MMS magnetometer data collected during the events, referred to as “in-sample” data records.

The consistency between the SST19 reconstructions and the IDR observations motivates further validation of the DM approach (described in Section 2.1) and the corresponding magnetic field architecture (Section 2.2). In particular, it is important to verify that the SST19 magnetic field is sufficiently flexible to capture the topological changes of the tail magnetic field. Section 3 benchmarks the model architecture against known magnetic field distributions that contain magnetotail X- and O-lines. It is also important to quantify the IDR matching quality for future comparison with other similar reconstructions. The following section, Section 4, addresses this by augmenting Stephens et al. (2023) analysis with an additional 29 months of MMS magnetometer data while also excluding data from the event being reconstructed, so-called out-of-sample reconstructions, thus quantifying the degree to which the in-sample records aid reconstruction accuracy. Section 5 performs a bootstrapping analysis of one of the events, thus quantifying SST19's sensitivity to sampling noise. The findings are summarized in Section 6.

2. Methodology: SST19 Data Mining Reconstruction of the Magnetotail

The data mining (DM) based empirical reconstruction algorithm employed here largely matches that of earlier substorm reconstructions (Motoba et al., 2022; Sitnov, Stephens, et al., 2019; Stephens et al., 2019, 2023; Turner et al., 2021). The algorithm is comprised of two primary components: The first being the DM aspect (Section 2.1), in which the entire space magnetometer archive is mined for records from times similar to the particular time step being reconstructed, which imparts the time-dependence to the reconstructed magnetic and current density field, while the second component (Section 2.2) consists of the analytical structure that describes the morphology of the primary magnetospheric current systems and their associated magnetic fields. The formulation of the model architecture descends from the modular approach (Tsyganenko, 2013; Tsyganenko, Andreeva, Kubyshkina, et al., 2021), in which the total magnetic field is decomposed into a superposition of fields generated by individual sources: $\mathbf{B}_{\text{tot}} = \mathbf{B}_{\text{int}} + \mathbf{B}_{\text{ext}}$. $\mathbf{B}_{\text{int}}$ is the magnetic field generated by currents internal to the Earth, commonly represented by the International Geomagnetic Reference Field (IGRF) model (Alken et al., 2021), while $\mathbf{B}_{\text{ext}}$ corresponds to fields produced by currents external to the planet, here, assumed to be magnetospheric in origin: $\mathbf{B}_{\text{ext}} = \mathbf{B}_{\text{eq}} + \mathbf{B}_{\text{FAC}} + \mathbf{B}_{\text{MP}}$, where $\mathbf{B}_{\text{eq}}$, $\mathbf{B}_{\text{FAC}}$, and $\mathbf{B}_{\text{MP}}$ are the magnetic fields due to the equatorial, field-aligned, and magnetopause currents respectively. Classic modular models further decomposed the equatorial currents, for example, into their contributions from the symmetric ring current (SRC), partial ring current (PRC), and tail current (e.g., Tsyganenko & Sitnov, 2005). However, beginning with Tsyganenko and Sitnov (2007), a new approach was leveraged which instead represented the magnetic field of the equatorial currents using a flexible basis-function expansion, allowing the morphology and interaction between the SRC, PRC, and tail current to be dictated by the data. A flexible FAC description would later be adopted as well (Sitnov et al., 2017).

2.1. Dynamic Evolution Using Data Mining

The analytical structure of the model contains several free variables (detailed in Section 2.2), including linear amplitude coefficients, which determine the magnitude of the magnetic field systems, along with non-linear parameters, which typically describe the physical properties of the current systems such as their location and size, both of which are determined by fitting them to magnetometer data. The time dependence arises from generalizing these variables to be functions of time. The earliest empirical magnetic field models simply binned the available magnetometer data by the *Kp* index and performed separate fits for each bin (Mead & Fairfield, 1975; Tsyganenko, 1989). Subsequent models instead employed dynamical response functions, where the free variables in the analytical model structure were themselves made functions of solar wind conditions and geomagnetic indices (Tsyganenko, 1996, 2002b; Tsyganenko & Andreeva, 2015; Tsyganenko & Sitnov, 2005). A new DM approach was devised by Sitnov et al. (2008). For each time step, originally at a 1-hr and later upgraded to a 5-min cadence, during a storm the entire archive of space magnetometer data is mined for a small subset of data from other events when the magnetosphere was in a similar storm state based on the storm index *Sym* - H, its time derivative, along with a proxy for the solar wind driving vB_z^{IMF}. This approach was later applied to substorms by also adding the substorm index *AL* and its time derivative to the state space (Stephens et al., 2019), termed SST19. Subsequent studies would use the SuperMAG analogs (Gjerloev, 2012) for the storm, *SMR* (Newell & Gjerloev, 2012), and substorm, *SML* (Newell & Gjerloev, 2011), indices.

2.1.1. k-Nearest Neighbors Method and Fitting Procedure

Storms and substorms represent repeatable dynamical responses of the magnetosphere due to solar wind driving, and their aggregate effect, as observed by ground-based magnetometers, can be distilled down to metrics termed geomagnetic indices (e.g., Liemohn et al., 2018; Menvielle et al., 2010). Based on the systems theory approach (Vassiliadis, 2006), the DM algorithm presupposes that the combined global storm and substorm state of the magnetosphere can be characterized using a small number of state variables, termed a state space. For any given time step, the current storm/substorm state of the magnetosphere corresponds to a state-vector within this state space, $\mathbf{G}(t)$. As a storm and/or substorm progresses, $\mathbf{G}(t)$ will trace out a trajectory within this state space, and similar storms and/or substorms will trace similar trajectories. In this way, the state space is conceptually similar to the phase space in Hamiltonian dynamics (Goldstein & Safko, 2002). As such, it is crucial to include not only geomagnetic indices but also their time derivatives. The state space utilized here is identical to that of Stephens et al. (2023). The combined storm and substorm state of the magnetosphere is represented by the 5D state vector, $\mathbf{G}(t)$, where the components are composed of the *SMR* and *SML* indices, their time derivatives, and the degree of solar wind driving reflect by $vB_{\mathrm{s}}^{\mathrm{IMF}}$, where, as described before, v is the opposite of the x-component of the solar wind velocity and $B_{\mathrm{s}}^{\mathrm{IMF}}$ is the southward component of the IMF defined as $B_{\mathrm{s}}^{\mathrm{IMF}} = -B_z^{\mathrm{IMF}}$ when $B_z^{\mathrm{IMF}} < 0$ and $B_{\mathrm{s}}^{\mathrm{IMF}} = 0$ otherwise. The 1-min time series for *SMR* and *SML* were obtained from the SuperMAG (Gjerloev, 2012) webpage (https://supermag.jhuapl.edu/indices) while the data describing the solar wind conditions ($v, B_z^{\mathrm{IMF}}, P_{\mathrm{dyn}}$) were obtained from 5-min OMNI data (Papitashvili & King, 2020). Each component of the 5D state space is smoothed in time, the *SMR* index is pressure-corrected to remove contributions from the magnetopause and induction currents (Gonzalez et al., 1994; Tsyganenko, Andreeva, Sitnov, et al., 2021), and discretized by sampling at a 5-min cadence as is detailed in Stephens et al. (2023).

To illustrate the workings of the DM algorithm, consider a particular query time step, $t = t^{(\mathrm{q})}$, for which a reconstruction is sought. This corresponds to a state-vector, $\mathbf{G}^{(\mathrm{q})} = \mathbf{G}\left(t^{(\mathrm{q})}\right)$, in the 5D state space. Surrounding this state vector in the state space will be other state vectors from similar dynamical events when the magnetosphere was presumably in a similar global storm/substorm configuration. This subset of similar points, $\mathbf{G}^{(i)}$, is termed the k-nearest neighbors (NNs), where the number of points in the subset is given by k_{NN}. Thus, the algorithm resembles the kNN lazy learning classification method (e.g., Wettschereck et al., 1997). The proximity between the query point, $\mathbf{G}^{(\mathrm{q})}$, and the NNs, $\mathbf{G}^{(i)}$, is defined using the Euclidean distance metric,

$$R_{\mathrm{q}}^{(i)} = \sqrt{\sum_{k=1}^{5} \left(\frac{G_k^{(\mathrm{q})} - G_k^{(i)}}{\sigma_{G_k}} \right)^2}, \tag{1}$$

where each component of $\mathbf{G}$ is standardized by dividing by its standard deviation, σ_{G_k}, computed over the entire state space. Note that standardization does not require subtracting the mean, as is done with the z-score, since the component differences are computed in Equation 1. The subset of NNs in state space has a corresponding subset of magnetometer records, $\mathbf{B}_j^{(\mathrm{obs})}$ observed at the locations $\mathbf{r}_j^{(\mathrm{obs})}$, from the space magnetometer archive (described below). Generally, the number of NN magnetometer records, S_{NN}, is not equal to the number of NNs in state space, k_{NN}, as there can be multiple spacecraft records for a given NN (recall each NN in the state space corresponds to a time step). The 432 linear amplitude coefficients and 10 non-linear parameters defining the SST19 architecture (Section 2.2) are then fit by minimizing the weighted root-mean-square differences between the SST19 reconstructed (modeled) magnetic field, $\mathbf{B}_j^{(\mathrm{mod})} = \mathbf{B}_{\mathrm{tot}}\left(\mathbf{r}_j^{(\mathrm{obs})}\right)$, and the observed field, $\mathbf{B}_j^{(\mathrm{obs})}$, over the subset of S_{NN} magnetometer records:

$$Q = \sqrt{\frac{\sum_{j=1}^{S_{\mathrm{NN}}} w_j^{(\mathrm{RS})} w_j^{(\mathrm{SS})} \varepsilon_j^2}{\sum_{j=1}^{S_{\mathrm{NN}}} w_j^{(\mathrm{RS})} w_j^{(\mathrm{SS})}}}, \tag{2}$$

$$\varepsilon_j^2 = \left(B_{j,x}^{(\mathrm{obs})} - B_{j,x}^{(\mathrm{mod})}\right)^2 + \left(B_{j,y}^{(\mathrm{obs})} - B_{j,y}^{(\mathrm{mod})}\right)^2 + \left(B_{j,z}^{(\mathrm{obs})} - B_{j,z}^{(\mathrm{mod})}\right)^2 \tag{3}$$

where the weighting functions, $w_j^{(\mathrm{SS})}$ and $w_j^{(\mathrm{RS})}$, apply weights based on the distance in the state space and real space, respectively. The latter, $w_j^{(\mathrm{RS})}(r)$, accounts for the inhomogeneity of data as a function of radius thereby weighting each record such that the total weight as a function of r is roughly constant, that is, records from regions with a large density of data are given smaller weights while records from sparse regions are given larger weights, as is described in Tsyganenko and Sitnov (2007). The former, $w_j^{(\mathrm{SS})}$, distance-weights the magnetometer records based on their distance to the query point (the time step being reconstructed) in state space, with NNs closer to the query point receiving larger weights (Sitnov et al., 2020; Stephens et al., 2020). The state space-based weighting is defined using a Gaussian function:

$$w_j^{(\mathrm{SS})} = \exp\left[-\frac{1}{2}\left(\frac{R_q^{(j)}}{\sigma R_{\mathrm{NN}}}\right)^2\right], \tag{4}$$

where R_{NN} is the radius of the NN hypersphere, that is, the distance of the farthest NN from the query point in state space: $R_{\mathrm{NN}} = \max\left(R_q^{(j)}\right)$. The variable σ determines the width of the Gaussian function. Larger values ($\sigma \gtrapprox 1$) negate the impact of distance-weighting, while smaller values ($\sigma \lessapprox 0.2$) effectively remove the farthest NNs from the fit due to their near-zero weights, which risks overfitting. Previous studies found that $\sigma = 0.3$ improves reconstruction fidelity while minimizing overfitting (Stephens et al., 2020), and, as such, this value is retained here. Note, magnetometer records taken concurrently with the reconstruction time step, $t = t^{(q)}$, the in-sample records, will receive the largest possible value of $w_j^{(\mathrm{SS})} = 1$ since $R_q^{(j)} = 0$. The objective function, Equations 2 and 3, is minimized by applying the singular value decomposition pseudo-inversion method to the over-determined linear least squares problem (Jackson, 1972; Press et al., 1992) to determine the linear amplitude coefficients, which are nested within the Nelder-Mead downhill simplex algorithm (Nelder & Mead, 1965) to solve for the non-linear parameters.

2.1.2. Space Magnetometer Archive

This study utilizes the space magnetometer archive from Stephens et al. (2023) except that the MMS portion (Russell et al., 2016; Torbert et al., 2016) of the archive was extended. The archive consists of magnetospheric spacecraft magnetometer observations beginning in the year 1995, approximately coinciding with the availability of nearly continuous L1 solar wind monitoring by the Wind spacecraft. The archive inherits data from IMP-8, Geotail (Kokubun et al., 1994), the Geosynchronous GOES-8, 9, 10, and 12 satellites (Singer et al., 1996) compiled for Tsyganenko and Sitnov (2007), which is averaged to a 15-min resolution through the end of 2005. This was later augmented to include Polar (Russell et al., 1995), Cluster (Balogh et al., 2001), THEMIS (Auster et al., 2008), and Van Allen Probes (Kletzing et al., 2013) data averaged to a 5-min resolution covering until the end of 2015 (Stephens et al., 2016; Stephens et al., 2019). Subsequent studies would also add MMS data to the archive, which proved critical in resolving the $B_z = 0$ nT isocontours associated with magnetotail reconnection sites (Sitnov, Stephens, et al., 2019; Stephens et al., 2023). Here, the MMS data set has been augmented again to include MMS data through May 2023, using a 5-min averaging cadence. Several filters have been applied to the magnetometer records, including limiting the data to observations taken when the spacecraft was inside the magnetopause boundary, determined either by visual inspection or via an empirical magnetopause model (e.g., Shue et al., 1998). Data from equatorial orbiting spacecraft are excluded when $r < 1.5R_E$ to remove potentially noisy measurements associated with spacecraft attitude uncertainties, while data from polar-orbiting satellites use a larger radial filter, $r < 3.2R_E$, to remove the large magnetic field deviations caused by low-altitude FACs. The final filter only allows data within $r < 36.0R_E$ to avoid biasing the reconstructions with sparse data beyond this distance. In total, the archive consists of 9,220,244 time-averaged magnetospheric magnetometer records spanning radial distances $1.5R_E \le r \le 36.0R_E$, 1,816,238 of which are from MMS, representing a 46% increase in the quantity of MMS data compared to Stephens et al. (2023).

2.2. SST19 Architecture

2.2.1. Equatorial Current System

The foundation for the magnetic field description of the equatorial current systems is the magnetic vector potential solution of a current sheet derived in Tsyganenko and Sitnov (2007): $\mathbf{B}_{\text{sheet}} = \nabla \times \mathbf{A}_{\text{sheet}}$. The solution comes about by assuming an infinitely thin current sheet in cylindrical coordinates (ρ, ϕ, z), thus allowing its magnetic field to be represented as a scalar potential, γ_{sheet}, whose form takes the general solution to Laplace's equation. Using the method from Stern (1987), the equivalent vector potential, $\mathbf{A}_{\text{sheet}}$, is found from γ_{sheet}. Although this solution is only valid for an infinitely thin current sheet, now that it is represented as a vector potential, a finite thickness is imparted by making the variable substitution $\zeta = \sqrt{z^2 + D^2}$, introducing a characteristic half-thickness parameter $D = D(\rho, \phi)$. The resulting magnetic field is a basis-function expansion taking the form

$$\mathbf{B}_{\text{sheet}}(\rho,\phi,z) = \sum_{n=1}^{N} a_{0n}^{(\text{s})}\mathbf{B}_{0n}^{(\text{s})} + \sum_{m=1}^{M}\sum_{n=1}^{N}\left(a_{mn}^{(\text{o})}\mathbf{B}_{mn}^{(\text{o})} + a_{mn}^{(\text{e})}\mathbf{B}_{mn}^{(\text{e})}\right), \tag{5}$$

where $\mathbf{B}_{0n}^{(\text{s})}$, $\mathbf{B}_{mn}^{(\text{o})}$, and $\mathbf{B}_{mn}^{(\text{e})}$ are basis functions possessing azimuthally symmetric, odd (sine), and even (cosine) symmetry respectively; while a_{mn} are the corresponding amplitude coefficients. To account for dynamic pressure effects on the equatorial current distribution, these amplitude coefficients are themselves made functions of P_{dyn} by replacing each one by $a_{\alpha\beta}^{(\gamma)} = a_{0,\alpha\beta}^{(\gamma)} + a_{1,\alpha\beta}^{(\gamma)}\sqrt{P_{\text{dyn}}}$, thus doubling their number. The values M and N dictate the number of expansions to be used and hence the spatial resolution of the equatorial current system, with M corresponding to the azimuthal resolution and N to the radial resolution. Here, as with previous applications of SST19, these hyperparameters are set to $(M, N) = (6, 8)$, corresponding to 208 linear coefficients. These (M, N) values allow the architecture to resolve the current systems associated with substorms in the near-tail and midtail (Stephens et al., 2019), such as the substorm current wedge, while limiting overfitting (Stephens & Sitnov, 2021).

2.2.2. Embedded Thin Current Sheet

During the substorm growth phase, the magnetotail develops a multiscale current sheet structure where an ion-scale thin current sheet (TCS) is embedded within the thicker plasma sheet (e.g., Artemyev & Zelenyi, 2012, and references therein). To mimic this structure, SST19 used two of the above equatorial expansions (Stephens et al., 2019):

$$\mathbf{B}_{\text{eq}} = \mathbf{B}_{\text{sheet,D}} + \mathbf{B}_{\text{sheet,D}_{\text{TCS}}}, \tag{6}$$

where $\mathbf{B}_{\text{eq,D}}$ represents the magnetic field due to the thicker plasma sheet while $\mathbf{B}_{\text{eq,D}_{\text{TCS}}}$ describes the embedded TCS. The original SST19 model assumed a spatially constant current sheet thickness for both current sheets, that is, $D = $ const and $D_{\text{TCS}} = $ const, with the constraint $D_{\text{TCS}} < D$, although they were allowed to vary as a function of time. However, if the physical mechanism of the emergence of the ion-scale TCS is the presence of figure-eight

Speiser (1965) proton orbits as theory suggests (Sitnov & Arnold, 2022, and refs. therein), then the structure of D_{TCS} should be spatially varying. This is because the orbit size of Speiser trajectories depends on the magnitude of the lobe magnetic field, which decreases with increasing distance along the magnetotail (Wang et al., 2004), meaning D_{TCS} should thicken at farther distances. To account for this effect, Stephens et al. (2023) utilized a form of D_{TCS} that monotonically increased with increasing ρ. This structure performed as anticipated throughout the magnetotail but resulted in the thinnest portion of the TCS residing near the planet. However, earthward of the transition region, the magnetic field morphology is categorically different from the magnetotail as the approximately dipolar internal field becomes the dominant magnetic field source. Therefore, here we adopt a different form of the TCS that allows a gradually thickening TCS at farther distances down the tail while also enabling a thicker TCS in the near-Earth region:

$$D_{\text{TCS}}(\rho,\phi) = D_0 \tanh(\beta\rho) + \alpha \exp(-\epsilon\rho). \tag{7}$$

The first term, $D_0 \tanh(\beta\rho)$, represents a monotonically increasing thickness asymptotically approaching the thickness value D_0 at large ρ. The parameter β regulates how quickly, as a function of ρ, the thickness approaches D_0. The second term, $\alpha \exp(-\epsilon\rho)$, acts to thicken the TCS in the near-Earth region, where the parameter α determines how thick the near-Earth TCS gets while ϵ determines how quickly, as a function of ρ, the near-Earth TCS thickens.

2.2.3. Additional Details

This description of the equatorial current system presupposes that it is centered about the equatorial (x-y) plane. In reality, non-zero values of the dipole tilt angle and B_y^{IMF} deform the location of the neutral sheet off the equatorial plane (Tsyganenko et al., 2015; Tsyganenko & Fairfield, 2004; Xiao et al., 2016). To account for these effects, the equatorial magnetic field is deformed via application of the general deformation technique (Tsyganenko, 1998), specifically by using the "bowl-shaped" deformation (Tsyganenko, 2014; Tsyganenko & Andreeva, 2014). This introduces three more non-linear parameters which describe $\mathbf{B}_{\text{eq}}$: the hinging distance R_{H} which controls the degree of bending in the x-z plane, the warping parameter G which warps the equatorial current sheet in the y-z plane, and the twist parameter TW which rotates the current sheet about the x-axis.

In summary, the architecture for the magnetic field, $\mathbf{B}_{\text{eq}}$, generated by equatorial currents contains 416 linear amplitude coefficients and eight non-linear parameters: D, D_0, α, β, ϵ, R_{H}, G, and TW. Other elements of the SST19 description of the magnetic field include those generated by field-aligned currents (FACs) and magnetopause currents, $\mathbf{B}_{\text{FAC}}$ and $\mathbf{B}_{\text{MP}}$ respectively, along with the expansion and contraction of the magnetosphere in response to changes in the solar wind dynamic pressure, P_{dyn}. These elements remain unchanged from all previous SST19 versions and introduce 16 additional linear amplitude coefficients and 2 non-linear parameters, κ_{R1} and κ_{R2}, which determine the spatial size, and thereby the latitudinal range, of the region-1 and region-2 FACs respectively (Sitnov, Stephens, et al., 2019; Stephens et al., 2019, 2023).

3. Benchmarking the Model Architecture Using Prescribed Magnetic Field Distributions

To validate and benchmark that the SST19 architecture and its corresponding equatorial spatial resolution can reconstruct global-scale X- and O-lines, the model is fit to a prescribed magnetic field distribution containing an X- and O-line in the magnetotail. The prescribed distributions are constructed by inserting a disk current system into the magnetotail as is described in the next Section 3.1, while the fitting procedure is detailed in Section 3.2. This is performed for 100 randomly generated disks, and the comparison between the prescribed and reconstructed X- and O-lines is quantified in Section 3.3.

3.1. Prescribed Magnetic Field Distributions Containing Magnetotail X- and O-Lines

The prescribed magnetic field distribution is constructed by embedding a disk-like current system into the magnetotail of an earlier-generation empirical magnetic field model, as shown in Figure 1. The external field, $\mathbf{B}_{\text{ext}}$, is described using the T96 model (Tsyganenko, 1995, 1996). T96 is configured using typical values corresponding to a moderately driven magnetosphere: $P_{\text{dyn}} = 3$ nPa, $B_z^{\text{IMF}} = -4$ nT, and $Dst = -50$ nPa. For simplicity, North-South symmetry is preserved by setting the dipole tilt angle and the y-component of the IMF to

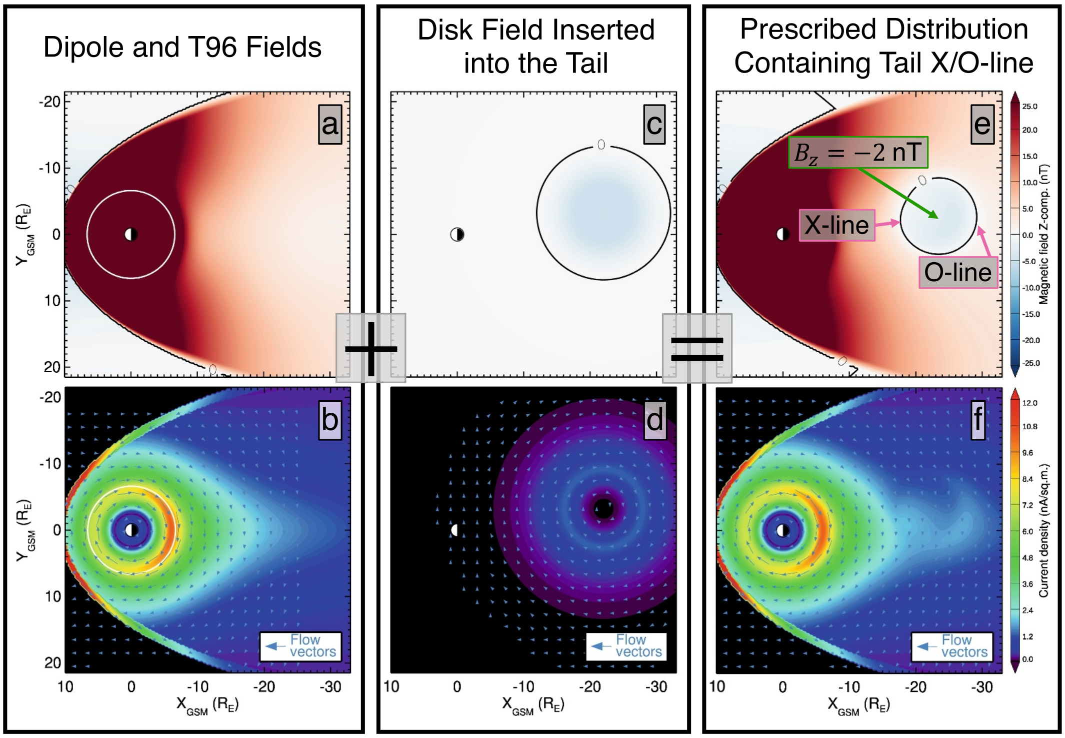

Figure 1. Prescribed magnetic field distribution containing an X- and O-line in the magnetotail. (a) The equatorial distribution of the z-component of the magnetic field of the T96 and dipole magnetic field models. (b) The corresponding equatorial distribution of the magnitude of the current density. The direction of the current density vectors is indicated by the overplotted arrows. Panels (c, d) The same as panels (a, b) but for a disk current system, Disk 29 in Figure S1 of Supporting Information S1, centered at $\mathbf{r}_0 = (-22.0, -3.2, 0.0)R_E$. The black line indicates the $B_z = 0$ isocontour. Panels (e, f) The same as panels (a, b) but for the combined field. The resulting distribution now contains an X- and an O-line indicated by the earthward and tailward edges of the black $B_z = 0$ isocontour. The magnitude of the disk current is scaled such that $B_z(\mathbf{r}_0) = -2$ nT.

zero: $\Psi = 0, B_y^{\mathrm{IMF}} = 0$, which also aligns the magnetic equator with the equatorial (x-y) plane. The internal field, $\mathbf{B}_{\mathrm{int}}$, is defined using the dipole approximation of the International Geomagnetic Reference Field (IGRF) (Alken et al., 2021) evaluated on 1 January 2010, 00:00. The combined T96 and dipole magnetic field distribution is shown in Figure 1a and the corresponding current density, $\mu_0 \mathbf{j} = \nabla \times \mathbf{B}$, distribution is displayed in Figure 1b. To this distribution, the magnetic field due to a westward flowing disk current system, $\mathbf{B}_{\mathrm{disk}}$ (Tsyganenko & Peredo, 1994), is added as shown in Figures 1c–1f.

The implementation of $\mathbf{B}_{\mathrm{disk}}$ is based on the disk-like current system used to describe the tail current in the T02 model (Tsyganenko, 2002a), where the magnetic field is defined to be the curl of the azimuthal magnetic vector potential given by

$$\begin{aligned} A_\phi(\rho,\phi,z) &= \rho \sum_{i=1}^{5} f_i \frac{t_i\sqrt{1-t_i^2}}{S_i^{(1)} S_i^{(2)}}, \\ t_i &= \frac{2b_i}{S_i^{(1)} + S_i^{(2)}}, \\ S_i^{(1)} &= \sqrt{(\rho + b_i)^2 + (\zeta + c_i)^2}, \\ S_i^{(2)} &= \sqrt{(\rho - b_i)^2 + (\zeta + c_i)^2}, \\ \zeta &= \sqrt{z^2 + {D_{\mathrm{disk}}}^2}. \end{aligned} \tag{8}$$

Table 1
Consistency Between the Reconstructed Magnetotail Magnetic Field and the IDR Location Observed by MMS

IDR	$\mathbf{r}_{\text{IDR}}$ (R_E)	$B^{(\text{in})}_{z,\text{IDR}}$ (nT)	$B^{(\text{out})}_{z,\text{IDR}}$ (nT)	$S^{(\text{in})}_{B_z}$	$S^{(\text{out})}_{B_z}$
A	(−19.3,−11.8, 0.8)	6.8(7.6)	8.9(8.5)	0.11	−0.05
B	(−17.6, 3.3, 1.7)	3.0(7.7)	3.8(8.2)	0.61	0.54
C	(−24.1, 1.4, 4.4)	0.8(3.5)	0.9(3.4)	0.77	0.74
D	(−24.2, 1.3, 4.5)	1.2(4.2)	2.4(4.2)	0.72	0.42
E	(−21.5, 4.1, 3.8)	1.0(3.4)	3.3(3.6)	0.70	0.09
F	(−18.1, 7.3, 0.7)	4.1(5.8)	4.1(5.9)	0.29	0.31
G	(−20.6, 9.1, 3.5)	0.2(5.8)	2.6(5.5)	0.97	0.52
H	(−22.9, 9.0, 2.3)	0.2(3.1)	1.5(3.0)	0.94	0.50
I	(−23.0, 8.9, 2.2)	1.8(3.7)	3.0(3.7)	0.51	0.19
J	(−18.9, 13.0, 0.4)	1.1(4.2)	1.3(4.2)	0.74	0.70
K	(−16.4, 4.4, 3.8)	3.9(4.2)	2.7(3.8)	0.07	0.29
L	(−18.8, 16.1, 1.1)	3.1(5.1)	6.7(5.0)	0.40	−0.35
M	(−19.2, 12.5, 1.6)	2.0(6.7)	8.0(5.8)	0.69	−0.36
N	(−9.5, 12.6, −0.1)	8.6(10.6)	9.2(11.1)	0.19	0.17
O	(−21.1, 13.3, 0.8)	−1.0(5.7)	5.1(5.5)	0.82	0.06
P	(−21.1, 13.1, 1.0)	1.0(5.5)	4.8(5.8)	0.81	0.18
Q	(−18.2, 15.9, 1.3)	−1.1(7.5)	−13.6(7.4)	0.86	−0.84
R	(−17.5, 12.7, 3.1)	−0.5(5.2)	2.1(5.4)	0.91	0.62
S	(−24.0, −8.3, 4.2)	0.6(4.3)	2.7(4.5)	0.86	0.39
T	(−13.0, 13.3, 0.4)	2.7(7.9)	4.7(8.2)	0.66	0.43
U	(−21.9, 6.5, −0.9)	0.5(4.1)	0.8(4.1)	0.88	0.80
V	(−28.1, −2.7, 3.5)	1.0(5.5)	1.7(5.6)	0.82	0.69
W	(−28.1, −2.8, 3.5)	1.6(4.8)	2.1(4.8)	0.67	0.57
X	(−27.5, −4.9, 1.5)	−0.9(4.3)	−1.9(4.3)	0.78	0.55
Y	(−25.0, 3.0, 4.6)	−0.1(3.9)	0.3(3.7)	0.98	0.92
Z	(−11.7, 11.2, 0.9)	5.5(4.5)	7.1(4.6)	−0.22	−0.54
Med	N/A	1.1(4.9)	2.9(4.9)	0.73	0.41

Note. The first column indicates the IDR event, labeled A–Z, while the second column states the location of MMS when the IDR was observed, in GSM coordinates (Rogers et al., 2019, 2023). The third and fourth columns show the z-component of the reconstructed magnetic field evaluated at the MMS location for the in-sample and out-of-sample reconstructions, respectively. The values inside the parentheses indicate the mean of these values due to random chance. The fifth and sixth columns display the skill score of the in-sample and out-of-sample reconstructions, respectively, compared to random chance. The last row shows the median of the columns over the 26 events, except the third and fourth columns evaluate the median of $\left|B^{(\text{in})}_{z,\text{IDR}}\right|$ and $\left|B^{(\text{in})}_{z,\text{IDR}}\right|$ respectively instead.

The values of f_i, b_i, and c_i were found by fitting the terms of the expansion to a prescribed current distribution as is detailed in Section 2.2 of Tsyganenko (2002a). The fit values are given in Table 1 of that work. The quantity D_{disk} defines the current sheet half-thickness of the disk, here assumed to be a constant of $D_{\text{disk}} = 2R_E$, where this value was chosen as it approximately matches the current sheet thickness of the tail current system in the T96 model. The disk current is further generalized to allow the size and center of the disk current system to change by modifying the position vector: $\mathbf{B}_{\text{disk}}(\mathbf{r}) = A_{\text{disk}}\mathbf{B}'_{\text{disk}}(\alpha(\mathbf{r} - \mathbf{r}_0))$, where $\mathbf{B}'_{\text{disk}}$ is the unmodified field given by the curl of Equation 8, $\mathbf{r}_0$ is the center of the disk current system, α is the rescaling factor, and A_{disk} is the amplitude coefficient. Setting $\alpha > 1$ shrinks the diameter of the current disk. For example, a current disk system configured with the values of $\mathbf{r}_0 = (-22.0,\ -3.2, 0.0)R_E$ and $\alpha = 2.63$ is displayed in Figures 1c and 1d. The amplitude of the system, $A_{\text{disk}} = 1.33$, is set to a value such that the z-component of the total magnetic field, $B_{\text{tot},z} = B_{\text{T96},z} + B_{\text{dip},z} + B_{\text{disk},z}$, evaluated at $\mathbf{r}_0$ is −2 nT, as is indicated in Figure 1e. The value $B_{\text{tot},z}(\mathbf{r}_0) = -2$

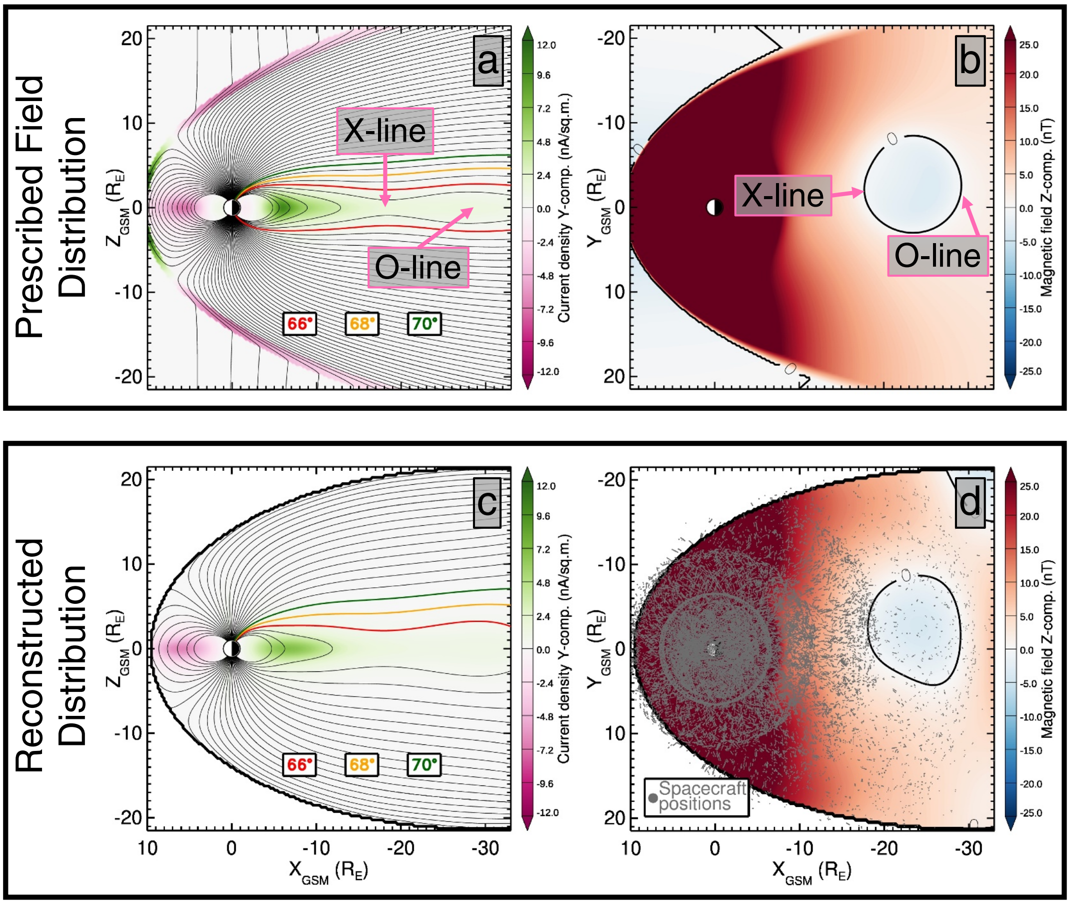

Figure 2. Fitting the SST19 architecture to a prescribed magnetic field distribution. (a) The meridional distribution of the y-component of the current density of the prescribed magnetic field containing an X- and an O-line as shown in Figure 1. Field lines, originating from the Earth's surface, are shown by the black lines, with select field lines colored as indicated. (b) The equatorial distribution of the z-component of the prescribed magnetic field containing an X- and O-line as indicated by the earthward and tailward edges of the black $B_z = 0$ isocontour. The panel is the same as (Figure 1e). (c, d) The resultant SST19 reconstructed magnetic field and current density distributions after fitting the SST19 architecture to the prescribed distribution. The set of spacecraft locations used to sample the prescribed distribution is shown by the gray circles in panel (d).

nT was chosen because it is a typical value of the magnetic field tailward of reconstructed X-lines, as reported in Stephens et al. (2023). For example, see their Figure 2, which shows that the regions of negative B_z associated with tail reconnection have typical values of -1 to -3 nT. The radius of this disk, defined as the distance from $\mathbf{r}_0$ to the site of the maximum current density magnitude, $\max(j_{\mathrm{disk}})$, is $r_{\mathrm{disk}} = 5.89R_E$.

The resulting combined magnetic field, $\mathbf{B}_{\mathrm{tot}} = \mathbf{B}_{\mathrm{T96}} + \mathbf{B}_{\mathrm{dip}} + \mathbf{B}_{\mathrm{disk}}$, and its corresponding current density are shown in Figures 1e and 1f. It demonstrates how the embedded current disk generates a roughly circular region within the tail where $B_{\mathrm{tot},z} < 0$. The black contour represents the $B_{\mathrm{tot},z} = 0$ isocontour. The earthward edge of this isocontour corresponds to a magnetic X-line while its tailward boundary marks the location of an O-line. This structure approximates the reconstructed magnetic field distribution during IDR events (Stephens et al., 2023).

3.2. Fitting SST19 to Prescribed Distributions

The above-described prescribed magnetic field distributions can now be utilized to qualitatively and quantitatively benchmark the degree to which the SST19 empirical magnetic field model architecture described in Section 2.2 is capable of reconstructing magnetotail reconnection sites. SST19 is fit by sampling the prescribed magnetic field at a representative distribution of spacecraft locations identified using the DM procedure described in Section 2.1, specifically, the set of locations used to reconstruct the observed IDR during Event H, 2017-207 (26 July) 07:00, from Stephens et al. (2023). In particular, see their Figure 6e showing the distribution of spacecraft locations (gray dots) in the equatorial (x-y) plane. Any spacecraft locations located beyond the T96 magnetopause are discarded. The fitting procedure follows the one described in Section 2.1.1 but with some modifications. First, the observed magnetic field vectors, $\mathbf{B}_j^{(\mathrm{obs})}$ in Equations 2 and 3, are replaced by evaluating the prescribed magnetic field at the sample spacecraft locations, $\mathbf{r}_j^{(\mathrm{obs})}$. Second, to avoid repeatedly refitting the non-linear parameters, which is computationally expensive, particularly for the next section where 100 randomly generated distributions are fit, a constant set of parameters is used while fitting each tail X- and O-line distribution. This set of non-linear parameters is determined by sampling the T96 field distribution without a disk current system (Figure 1a). Afterward, the linear amplitude coefficients are found by sampling the combined T96 and disk current systems. Third, as dipole tilt-related deformation effects are not considered in this section, the non-linear parameters R_{H}, G, and TW are irrelevant and were excluded from the fit. Finally, in this context the weights described in Equation 4 do not have a precise meaning and to more accurately mimic the distribution of weights from a real event, the same weights were assigned to each magnetometer vector that was determined when fitting the IDR from Event H, 2017-207 (26 July) 07:00. Note, the SST19 architecture contains an embedded TCS as is described by Equation 6. As the T96 model does not include this embedded TCS structure, it was found while fitting the non-linear parameters that the thickness of the thick current sheet became very large, $D = 15.5R_E$, thus making its contribution to the reconstructed magnetic field negligible.

Figure 2 displays the result of fitting the SST19 model architecture to the prescribed magnetic field distribution shown in Figure 1, comparing the prescribed magnetic field and current density distributions (top panels) to the reconstructed distributions (bottom panels). The locations of the spacecraft used to sample the prescribed field are indicated by the gray dots in Figure 2d. Generally, the reconstructed distributions, including the location of the $B_z = 0$ isocontour, match the prescribed ones. There are some notable differences. First, the T96 model features a penetrating IMF field module, as evident in the magnetic field lines that cross through the magnetopause boundary in Figure 2a. The inclusion of this field also generates Chapman-Ferraro currents. In contrast, the domain over which SST19 is valid is confined to inside the magnetopause. Second, SST19 underresolves the inner magnetosphere, including the magnitude of the westward ring current and the location and magnitude of the eastward ring current. This is expected because the number of expansions included in the description of the equatorial current system, $(M,N) = (6,8)$ from Equation 5, was chosen to prevent overfitting the tail region, thereby underresolving the inner magnetosphere, as was discussed in detail in Stephens and Sitnov (2021). Third, the reconstructed B_z distribution contains a spurious region of negative B_z as shown in the upper right of Figure 2d. This region contains no spacecraft locations; therefore, the reconstructed field is unconstrained by data. More generally, the spacecraft magnetometer archive used here, described in Section 2.1.2, contains little data beyond the apogee of the Geotail mission at $r = 31R_E$. For this reason, we restrict the benchmarking and validation analysis to $r \leq 31R_E$.

3.3. Uncertainty Quantification Using Randomly Generated Magnetotail X- and O-Lines

To quantitatively assess SST19's fidelity at reconstructing a variety of magnetotail X- and O-lines, the above analysis is repeated using 100 randomly generated disk currents embedded into the T96 magnetic field. The disk centers, $\mathbf{r}_0$, are randomly selected from a uniform distribution ranging from $x = [-35, -10]R_E$, $y = [-20, 20]R_E$, $z = 0R_E$. The size of the disks is determined by randomly sampling $1/\alpha$ from $[0.05, 1]$ again using a uniform distribution, corresponding to disk radii, r_{disk}, ranging from ≈ 1 to $14.5R_E$. An additional filter is added to ensure that each disk is primarily located within the magnetopause by requiring $|r_{0,y}| + r_{\mathrm{disk}} < 20R_E$. As described in Section 3.1, the amplitude of each disk, A_{disk}, is selected such that the $B_{\mathrm{tot},z}(\mathbf{r}_0) = -2$ nT. Figure 3 displays the first 20 randomly prescribed magnetic field distributions with the resulting X- and O-lines indicated by the black $B_z = 0$ isocontours with the variables defining the disk current systems, $\mathbf{r}_0$, α, A_{disk}, and r_{disk}, shown in the upper left-hand text box of each panel. The SI includes the remaining 80 prescribed magnetic field distributions in Figures S1–S4 in Supporting Information S1.

Using the procedure described in Section 3.2, the SST19 magnetic field architecture is fit to the prescribed magnetic field distribution of each of the 100 randomly generated magnetotail X- and O-lines. The purple $B_z = 0$ isocontours in Figure 3 (and Figures S1–S4 in Supporting Information S1) compare the fit X- and O-lines to the prescribed ones. Of the 100, 23 are not successfully reproduced by fitting the SST19 architecture, meaning no $B_z = 0$ nT isocontour is reconstructed in the vicinity of the prescribed isocontour. There is a clear relationship between the radius of the disk and SST19's capacity to reconstruct a region of negative B_z, with the smaller disks generally corresponding to failed reconstructions. Of the 15 disks with $r_{\mathrm{disk}} < 2.5R_E$, only one (Disk 059) is

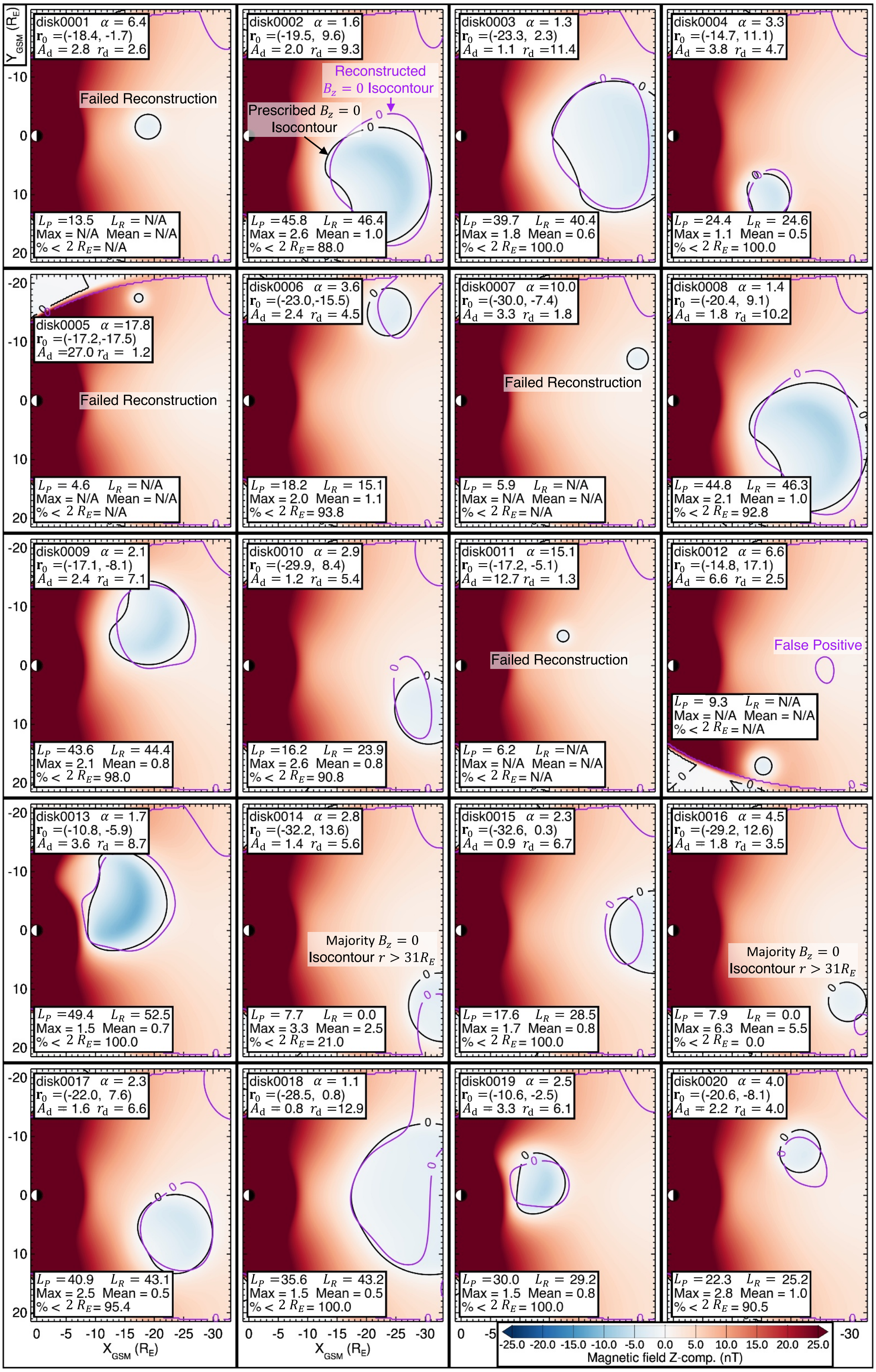
Y_{GSM} (R_E)
disk0001 α = 6.4 $\mathbf{r}_0$ =(-18.4, -1.7) A_d = 2.8 r_d = 2.6
Failed Reconstruction
L_P =13.5 L_R = N/A Max = N/A Mean = N/A % < 2 R_E= N/A
disk0002 α = 1.6 $\mathbf{r}_0$ =(-19.5, 9.6) A_d = 2.0 r_d = 9.3
Reconstructed B_z = 0 Isocontour
Prescribed B_z = 0 Isocontour
L_P =45.8 L_R = 46.4 Max = 2.6 Mean = 1.0 % < 2 R_E= 88.0
disk0003 α = 1.3 $\mathbf{r}_0$ =(-23.3, 2.3) A_d = 1.1 r_d =11.4
L_P =39.7 L_R = 40.4 Max = 1.8 Mean = 0.6 % < 2 R_E= 100.0
disk0004 α = 3.3 $\mathbf{r}_0$ =(-14.7, 11.1) A_d = 3.8 r_d = 4.7
L_P =24.4 L_R = 24.6 Max = 1.1 Mean = 0.5 % < 2 R_E= 100.0
disk0005 α =17.8 $\mathbf{r}_0$ =(-17.2,-17.5) A_d =27.0 r_d = 1.2
Failed Reconstruction
L_P = 4.6 L_R = N/A Max = N/A Mean = N/A % < 2 R_E= N/A
disk0006 α = 3.6 $\mathbf{r}_0$ =(-23.0,-15.5) A_d = 2.4 r_d = 4.5
L_P =18.2 L_R = 15.1 Max = 2.0 Mean = 1.1 % < 2 R_E= 93.8
disk0007 α =10.0 $\mathbf{r}_0$ =(-30.0, -7.4) A_d = 3.3 r_d = 1.8
Failed Reconstruction
L_P = 5.9 L_R = N/A Max = N/A Mean = N/A % < 2 R_E= N/A
disk0008 α = 1.4 $\mathbf{r}_0$ =(-20.4, 9.1) A_d = 1.8 r_d =10.2
L_P =44.8 L_R = 46.3 Max = 2.1 Mean = 1.0 % < 2 R_E= 92.8
disk0009 α = 2.1 $\mathbf{r}_0$ =(-17.1, -8.1) A_d = 2.4 r_d = 7.1
L_P =43.6 L_R = 44.4 Max = 2.1 Mean = 0.8 % < 2 R_E= 98.0
disk0010 α = 2.9 $\mathbf{r}_0$ =(-29.9, 8.4) A_d = 1.2 r_d = 5.4
L_P =16.2 L_R = 23.9 Max = 2.6 Mean = 0.8 % < 2 R_E= 90.8
disk0011 α =15.1 $\mathbf{r}_0$ =(-17.2, -5.1) A_d =12.7 r_d = 1.3
Failed Reconstruction
L_P = 6.2 L_R =N/A Max = N/A Mean = N/A % < 2 R_E= N/A
disk0012 α = 6.6 $\mathbf{r}_0$ =(-14.8, 17.1) A_d = 6.6 r_d = 2.5
False Positive
L_P = 9.3 L_R = N/A Max = N/A Mean = N/A % < 2 R_E= N/A
disk0013 α = 1.7 $\mathbf{r}_0$ =(-10.8, -5.9) A_d = 3.6 r_d = 8.7
L_P =49.4 L_R = 52.5 Max = 1.5 Mean = 0.7 % < 2 R_E= 100.0
disk0014 α = 2.8 $\mathbf{r}_0$ =(-32.2, 13.6) A_d = 1.4 r_d = 5.6
Majority B_z = 0 Isocontour $r > 31 R_E$
L_P = 7.7 L_R = 0.0 Max = 3.3 Mean = 2.5 % < 2 R_E= 21.0
disk0015 α = 2.3 $\mathbf{r}_0$ =(-32.6, 0.3) A_d = 0.9 r_d = 6.7
L_P =17.6 L_R = 28.5 Max = 1.7 Mean = 0.8 % < 2 R_E= 100.0
disk0016 α = 4.5 $\mathbf{r}_0$ =(-29.2, 12.6) A_d = 1.8 r_d = 3.5
Majority B_z = 0 Isocontour $r > 31 R_E$
L_P = 7.9 L_R = 0.0 Max = 6.3 Mean = 5.5 % < 2 R_E= 0.0
disk0017 α = 2.3 $\mathbf{r}_0$ =(-22.0, 7.6) A_d = 1.6 r_d = 6.6
L_P =40.9 L_R = 43.1 Max = 2.5 Mean = 0.5 % < 2 R_E= 95.4
disk0018 α = 1.1 $\mathbf{r}_0$ =(-28.5, 0.8) A_d = 0.8 r_d =12.9
L_P =35.6 L_R = 43.2 Max = 1.5 Mean = 0.5 % < 2 R_E= 100.0
disk0019 α = 2.5 $\mathbf{r}_0$ =(-10.6, -2.5) A_d = 3.3 r_d = 6.1
L_P =30.0 L_R = 29.2 Max = 1.5 Mean = 0.8 % < 2 R_E= 100.0
disk0020 α = 4.0 $\mathbf{r}_0$ =(-20.6, -8.1) A_d = 2.2 r_d = 4.0
L_P =22.3 L_R = 25.2 Max = 2.8 Mean = 1.0 % < 2 R_E= 90.5
-20 -10 0 10 20
0 -5 -10 -15 -20 -25 -30
X_{GSM} (R_E)
-25.0 -20.0 -15.0 -10.0 -5.0 0.0 5.0 10.0 15.0 20.0 25.0
Magnetic field Z-comp. (nT)

Figure 3.

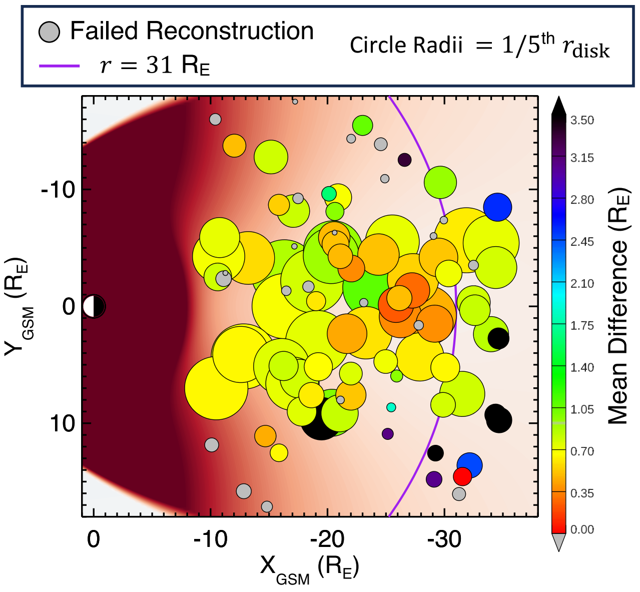

Figure 4. A summary of fitting the SST19 architecture to all 100 randomly generated magnetic field distributions. The equatorial distribution of the z-component of the T96 magnetic field (Figure 1a) is included in the background for context and is not associated with the color bar. Each colored circle is centered at $\mathbf{r}_0$ while its radius is $\frac{1}{5}$ of r_{disk}. The color of the circles represents the mean distance between the prescribed and reconstructed $B_z = 0$ nT isocontours, computed within $r < 31R_E$, which is indicated by the purple line. Failed reconstructions, those with no $B_z = 0$ nT isocontour in the vicinity of the prescribed isocontour, are shaded gray.

successfully reconstructed, while 21 of the 23 failed reconstructions have $r_{\text{disk}} < 3.5R_E$. Examples include Disks 001, 005, 007, 011, and 012 in Figure 3. The two other failed reconstructions (Disks 060 and 053), have $B_z = 0$ nT isocontours located nearly entirely beyond $r = 31R_E$ where the available data is sparse. Excluding these two, every disk with a radius $r_{\text{disk}} > 3.5R_E$ is successfully reconstructed. Disks 014 and 016 in Figure 3 demonstrate how the reconstruction algorithm struggles to resolve $B_z = 0$ nT isocontours located beyond $r = 31R_E$. Meanwhile, the prescribed $B_z = 0$ nT isocontours for Disks 006, 015, and 018 straddle $r = 31R_E$. The portions earthward of this boundary are well reproduced. Still, the tailward portions are not reproduced, causing the reconstructed B_z isocontours for Disks 006 and 018 to merge with the magnetopause and to squash Disk 015 along the x direction. Therefore, we can conclude the SST19 architecture and its equatorial resolution are generally incapable of resolving X-lines with short lengths $\lessapprox 2.5R_E$ but can reconstruct longer ones $\gtrapprox 3.5R_E$ as long as they occur where data is generally available.

To assess the fidelity of each reconstruction, the difference between the prescribed and reconstructed $B_z = 0$ nT isocontour is evaluated. To perform this, first both the prescribed and reconstructed $B_z = 0$ nT isocontours are found using a contouring algorithm with a discrete step size of $\frac{1}{8}R_E$. The lengths for each prescribed, L_{P}, and reconstructed, L_{R}, $B_z = 0$ nT isocontours are listed in the top row of the bottom left-hand text box in each panel of Figure 3 (and Figures S1–S4 in Supporting Information S1). In computing these lengths, as well as the other metrics displayed in text boxes, only the portion of the isocontour within $r < 31R_E$ is included. In cases where the isocontour intersects the magnetopause, the magnetopause boundary is used to evaluate its length instead. To compare the contours, each step of the prescribed $B_z = 0$ nT isocontour is traversed, and the minimum distance between that step and the reconstructed $B_z = 0$ nT isocontour is computed. The maximum and mean distances between the prescribed and reconstructed isocontours for each of the 100 randomly generated prescribed fields are reported in the middle row of each bottom left-hand text box. The last row in the text box indicates the percentage of the prescribed isocontour's length within $<2R_E$ of the reconstructed isocontour. Note that several of the prescribed $B_z = 0$ nT isocontours are located predominately or entirely beyond $31R_E$ (Disks 014, 016, 041, 051, 052, 055, 059, 084, 090), and, because the metrics are only computed for the portion of the isocontours within $r < 31R_E$, this leads to spurious values in the text boxes despite them being successful reconstructions. For example, see Disk 014 in Figure 3 where $L_{\text{P}} = 7.7R_E$ and $L_{\text{R}} = 0.0R_E$ as the majority of the prescribed and the entirety of the reconstructed isocontour lie beyond $31R_E$. Generally, discounting these problematic disks, the successful reconstructions have a maximum difference between the prescribed and reconstructed $B_z = 0$ nT isocontours of $<3R_E$, a mean difference of $<1R_E$, and $\gtrapprox 90\%$ of the reconstructed isocontour's length within $<2R_E$ of the prescribed one. Of the 100 reconstructed magnetic field distributions, three contained false positives (Disks 012, 069, and 89), that is, they possess $B_z = 0$ nT isocontours that were not near the prescribed ones (see the example of Disk 012 in Figure 3).

Figure 4 summarizes the results of this section showing: (a) SST19 is generally incapable of resolving small $\left(r_{\text{disk}} \lessapprox 2.5R_E\right)$ X- and O-lines but successfully reconstructs larger ones $\left(\gtrapprox 3.5R_E\right)$, (b) the successful reconstructions generally resolve the $B_z = 0$ nT isocontours to a high degree of fidelity with mean differences of $<1R_E$, and (c) SST19 struggles to resolve isocontours near or beyond the apogee of Geotail at $r = 31R_E$ where the data availability dramatically decreases.

Figure 3. Fitting the SST19 architecture to 100 randomly generated magnetic field distributions. The equatorial distributions of the z-component of the prescribed magnetic field, in a format similar to Figure 2b, for the first 20 (the additional 80 are shown in Figures S1–S4 in Supporting Information S1), are displayed. The black line indicates the prescribed $B_z = 0$ isocontour while the overplotted purple line shows the reconstructed $B_z = 0$ isocontour, similar to Figure 2d. The top text box displays the values of the variables defining the random disk, $\mathbf{r}_0$, α, A_{disk}, and r_{disk}, while the bottom text box shows metrics on the comparison between the prescribed and reconstructed $B_z = 0$ nT isocontour.

4. In-Sample Versus Out-of-Sample Reconstructions

Typically, the disciplines of statistics and mathematical modeling use the terms “in-sample” and “out-of-sample” in the context of model cross-validation (e.g., Anguita et al., 2012). To perform model cross-validation, the full data set is partitioned into a training set and a validation set. The model is fit or trained using data contained in the training set, and the resulting Goodness-of-Fit metrics are referred to as “in-sample” metrics. Meanwhile, the validation set is withheld as an independent source in measuring the resulting model's generalization performance, that is, how well the model can reproduce new or unseen data. Goodness-of-Fit metrics computed using the validation set are referred to as “out-of-sample.” The concepts of in-sample and out-of-sample testing are also used in the context of forecasting, where out-of-sample tests are generally considered the appropriate means for determining the accuracy of a forecasting method (Tashman, 2000). In the context of this study, in-sample event reconstructions are defined as those that use magnetometer records from the event itself in the fitting procedure from Section 2.1.1, while out-of-sample reconstructions contain no data within the NN subset from the event being reconstructed.

The prior study comparing the empirical magnetic field reconstructions of the magnetotail to the MMS-observed locations of IDRs relied on in-sample methods (Stephens et al., 2023). Even though the in-sample data points formed a relatively minuscule amount of the selected data for each reconstruction, on the order of dozens to a couple hundred data records out of the $\approx 9 \times 10^4$ total data records used for each reconstruction, these in-sample points could have a disproportionate impact on the reconstructions and their consistency with the MMS observed IDR locations. The reasons being: (a) the distance-weighting in the NN parameter space represented by Equation 4 necessarily gives the largest weights to records during the reconstructed time step, (b) the preponderance of records beyond the Cluster mission's primary apogee, $r \approx 18R_E$, are from MMS itself. Given these large weights and lack of non-MMS data in this region of the magnetotail, with Geotail being the only other mission that largely sampled here, the reconstructions may be drawn to or even overfit to match the observed location of the IDRs. This also has implications for the predictive nature of the DM reconstructions, that is, given the time series for the solar wind and geomagnetic indices used for the data mining procedure, how well does the DM algorithm predict the location of magnetotail reconnection, assuming no concurrent spacecraft observations? If the in-sample records are critical in providing consistency between the DM reconstructions and the location of the MMS IDRs, then the predictive capability of the DM algorithm in identifying the location of tail reconnection is low. To address these issues, here, we replicate the investigation of Stephens et al. (2023) with the primary difference being the new TCS structure defined by Equation 7 and the space magnetometer archive being augmented with an additional 29 months of MMS data. Here, all 26 (labeled events A–Z) MMS observed IDRs from Rogers et al. (2019, 2023) are reconstructed both with (in-sample reconstruction) and without (out-of-sample reconstruction) magnetometer records from the event itself. To implement the out-of-sample reconstructions, all magnetometer data records within ±2 hr of the time step being reconstructed were excluded, based on the typical substorm duration of ≈ 2 hr (Partamies et al., 2013). The in-sample reconstructions employed no such restriction and, given that magnetometer observations taken during the reconstructed event will be closest in the NN parameter space, each in-sample reconstruction utilized some MMS data from the event itself. The precise number of in-sample magnetometer records used for each in-sample reconstruction, and hence excluded from the out-of-sample reconstructions, varied, ranging from 12 (or 0.013% of all records) for Events V and W up to 188 (0.213% of all records) for Events A and N. Note, since the space magnetometer archive only includes MMS data after the year 2016 and the MMS survey of tail reconnection events began with the 2017 tail season, all in-sample records are MMS observations.

All 26 IDR event reconstructions, both in-sample and out-of-sample, were fit using the same set of initial non-linear parameters. The parameters defining the radially varying TCS structure, represented by Equation 7, were initialized to $D_0 = 3.2R_E$, $\alpha = 2.4R_E$, $\beta = 0.03$, and $\epsilon = 0.1$, while the initial half-thickness for the thick current sheet was set to $D = 3.5R_E$. These were chosen by exploring a range of different initial parameter values and observing where they tended to converge during the fitting procedure. Meanwhile, the initial parameters controlling the deformation of the equatorial current sheet were set to $R_\mathrm{H} = 8.14R_E$, $G = 2.6$, and $TW = 0.0$. The non-linear FAC parameters were initialized to $\kappa_\mathrm{R1} = 0.7$ and $\kappa_\mathrm{R2} = 0.83$. These values were chosen based on those resolved in prior studies (e.g., Stephens et al., 2023). Each reconstruction ran for 120 iterations or until convergence was reached. During the course of this investigation, the new TCS structure was found to be unstable when fit using a large number of iterations. That is, when finding the optimal set of non-linear parameters, the

Nelder-Mead downhill simplex method sometimes veers into nonphysical parameter spaces, an example being negative values for the current sheet thickness. For this reason, additional constraints were placed to ensure a physically consistent reconstruction. This was performed by evaluating D_{TCS} at varying values of ρ sampling the modeling domain: $\rho = 0.1, 1.0, 10.0, 20, 36.0 R_E$. The first constraint prevents the TCS from becoming overly thin or having negative values; at all sampled locations, the half-thickness of the TCS was constrained to be $D_{\text{TCS}} > D_{\text{TCS,min}}$, where $D_{\text{TCS,min}} = 0.4 R_E$. This constrained value is approximately the thinnest half-thickness resolved by Stephens et al. (2019), which used a spatially constant TCS. See, for example, their Figures 6f and 7f, which display the time series for D_{TCS} during a pair of substorms and a storm, respectively. The second constraint, as with previous studies (Sitnov, Stephens, et al., 2019; Stephens et al., 2019, 2023), requires the TCS to be thinner than the thick current sheet, $D_{\text{TCS}} < D$, where D is the half-thickness of the thick current sheet from Equation 6, at all sampled locations. A further constraint was imposed on the maximum thickness for $D < D_{\max}$, and thereby also D_{TCS}, where $D_{\max} = 5 R_E$. Third, assuming the thickness of the TCS is controlled by the lobe magnetic field, then the current sheet ought to get thicker at larger radial distances (e.g., Sitnov & Schindler, 2010). The constraint $D_{\text{TCS}}(\rho = 20 R_E) < D_{\text{TCS}}(\rho = 36 R_E)$ was added to capture this behavior. Finally, the primary motivation for adopting this new TCS structure was that the prior structure resulted in a monotonically increasing thickness of the TCS with increasing radial distance (Stephens et al., 2023), meaning the TCS was thinnest near the planet. This resulted in intense TCSs in the more dipolar inner magnetosphere, where the current sheet is expected to be thicker than in the tail region. To enforce this, the constraint that $D_{\text{TCS}}(\rho = 10 R_E) < D_{\text{TCS}}(\rho = 1 R_E)$ was added. These constraints were implemented by returning a large value in the objective function, Equations 2 and 3, thus forcing the Nelder-Mead simplex algorithm to avoid these nonphysical parameter spaces.

4.1. Qualitative Analysis of In-Sample and Out-of-Sample Reconstructions

Figures 5 and 6 compare the B_z equatorial distributions of the in-sample to the out-of-sample reconstructions for four of the 26 IDR events. For simplicity when plotting these distributions, the deformation of the equatorial current sheet due to dipole tilt and B_y^{IMF} effects is ignored by setting $\Psi = TW = 0$, which aligns the modeled neutral sheet with the equatorial plane. Figure 5 demonstrates two events (Event N and Event Y) where the in-sample and out-of-sample reconstructions are qualitatively similar based on the overall B_z equatorial distributions as well as the location of the $B_z = 0$ isocontour. Event N occurred during the late main phase of strong storm ($\min(SMRc) = -185$ nT) during a period of steady solar wind driving ($vB_z^{\text{IMF}} \approx -6$ mV/m) and shortly after a substorm onset which occurred at 06:20 UT (Forsyth et al., 2015) which would materialize into an intense substorm expansion ($\min(SML) = -2166$ nT). Meanwhile, the detection of the Event-Y IDR followed a period of weak solar wind driving and dynamic pressure ($P_{\text{dyn}} < 1$ nPa) shortly following substorm onset (14:40 UT), which would become a weak substorm ($\min(SML) = -105$ nT). In both events, the reconstructed field is consistent with the location of the observed IDR based on the equatorial distance to the $B_z = 0$ nT isocontour, $D_{0\text{nT}}$. $D_{0\text{nT}}$ is evaluated by projecting the IDR location to the equatorial (x-y) plane and determining the minimum distance to the reconstructed $B_z = 0$ nT isocontour while again ignoring deformation effects. For the in-sample reconstructions (Figures 5c1 and c2), $D_{0\text{nT}} = 1.9$ and $0.5 R_E$ for events N and Y respectively. Meanwhile, the out-of-sample reconstructions (Figures 5d1 and d2) possessed larger separations, $D_{0\text{nT}} = 2.5$ and $1.8 R_E$ for events N and Y respectively, but were still relatively consistent, $D_{0\text{nT}} < 2.5 R_E$, with the observed IDR location. The bottom pair of panels (Figures 5e1 and e2) displays the difference in the B_z equatorial distributions between the in-sample and out-of-sample reconstructions. The B_z differences for Event Y are relatively small, $|B_z| < 2$ nT, but are notably higher for Event N. This is perhaps because of the storm-time nature of Event N, which occurred during a period when the magnetosphere was compressed due to a high solar wind dynamic pressure, $P_{\text{pdyn}} = 7.83$ nPa, resulting in elevated values of $|B_z|$ throughout the magnetosphere compared to Event Y. However, Event Y's in-sample and out-of-sample B_z distributions are visually more distinct (compare Figure 5c2 to d2) compared to Event N, despite having lesser quantitative differences. For example, Event Y's in-sample $B_z = 0$ nT isocontour is shifted dawnward by several R_E relative to the out-of-sample one. The cause of this may be that Event Y's reconnection region is farther downtail where the data coverage is more sparse, thereby allowing the in-sample records to have a proportionally larger impact compared to Event N. Also, the reduced $|B_z|$ values throughout the magnetosphere in Event Y, compared to Event N, mean that smaller quantitative differences can have a larger visual impact.

Conversely, Figure 6 illustrates two events, G and M, where the out-of-sample reconstructions are qualitatively different and less consistent with the observed IDR location compared to the in-sample reconstructions. Event G

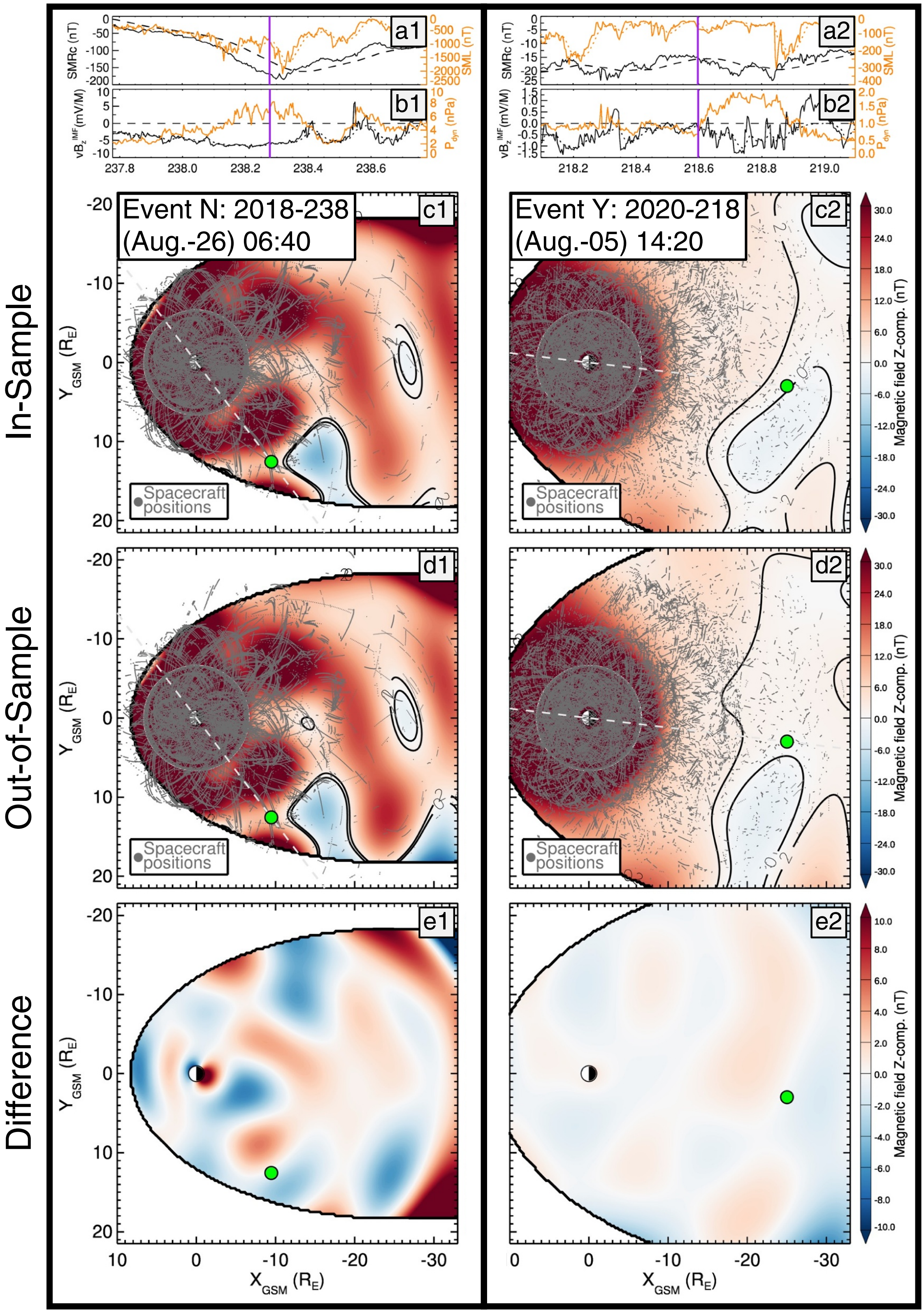
a1
SMRc (nT)
SML (nT)
b1
vB_z^{IMF} (mV/M)
P_{dyn} (nPa)
237.8
238.0
238.2
238.4
238.6
a2
b2
218.2
218.4
218.6
218.8
219.0
In-Sample
Event N: 2018-238 (Aug.-26) 06:40
c1
Event Y: 2020-218 (Aug.-05) 14:20
c2
Spacecraft positions
Out-of-Sample
d1
d2
Difference
e1
e2
Y_{GSM} (R_E)
X_{GSM} (R_E)
Magnetic field Z-comp. (nT)

Figure 5.

proceeded a period of moderate solar wind driving and occurred around the time of a substorm onset at 23:58 UT, although this substorm onset was embedded in the recovery phase of another moderately strong (min(SML) = −524 nT) substorm which began approximately 90 min earlier (onset 22:34 UT). Event M occurred during the middle of an approximately 2 hr long period of moderate solar wind driving ($vB_z^{\mathrm{IMF}} \approx -3$ mV/m) which generated a moderate storm (min($SMRc$) = −57 nT) but led to a strong substorm (min(SML) = −921 nT). The IDR was detected approximately half an hour after substorm onset (11:19 UT) during the early recovery phase. In both events, the in-sample reconstructions (Figures 6c1 and c2) contain regions with $B_z < 0$ in the vicinity of the observed IDR, which are not present in the out-of-sample reconstructions (Figures 6d1 and d2). Presumably, the relatively small number of in-sample records, 84 and 36 records for Events G and M, respectively, pulls the fitting results to match the observed IDR location for these events. These figures suggest that the global-scale location of some tail reconnection events is repeatedly correlated with the 5D parameter space while for other events it is not. The comparisons between the in-sample versus out-of-sample reconstructions for the remaining 22 IDR events are shown in Figures S5–S12 in Supporting Information S1 in a format similar to Figures 5 and 6.

Next, Figure 7 compares the MMS observed field (black line) to the in-sample (red line) and out-of-sample (blue line) reconstructed magnetic fields during the ±3 hr period when the IDR was observed for Events G and Y. The largest deviations between the reconstructed and observed fields appear in B_x. Although the in-sample field generally follows but underestimates the magnitude of the B_x variations, the out-of-sample reconstruction largely misses the B_x variations altogether. Event Y also includes a notable (≈10 nT) variation in B_y as well around 23:00–00:00, which again is more accurately, although not entirely, captured by the in-sample reconstruction. A potential cause of these variations is spontaneous North-South flapping motions of the current sheet, which have been observed in the magnetotail by MMS (Farrugia et al., 2021; Wang et al., 2019), which cannot be captured by SST19. In a reference frame fixed to the reconnection site, these flapping motions manifest as North-South deviations of the MMS trajectory as it traverses the reconnection site, resulting in oscillating B_x and B_y time series (e.g., Schroeder et al., 2022; Waters et al., 2025; Wei et al., 2019). Meanwhile, both the in-sample and out-of-sample reconstructions largely reproduce B_z (note the tighter range on panel c). Regardless, the out-of-sample reconstruction of Event G misses the B_z reversal observed at 00:00, thus causing the inconsistent reconstruction shown in Figure 6d1. At this time step, the MMS1 5-min averaged value is $B_z = -0.49$ nT while the out-of-sample value is $B_z = 2.6$ nT. The in-sample reconstruction also does not resolve the B_z reversal but comes significantly closer with a value of $B_z = 0.15$ nT. In contrast, the observed B_z for Event Y (Figure 7c2) shows no clear reversal at 5-min timescales and instead hovers near zero ($|B_z| \lessapprox 3$ nT) for several hours, which is largely reconstructed by both the in-sample and out-of-sample reconstructions equally well.

4.2. Uncertainty Quantification of In-Sample and Out-of-Sample Reconstructions

Next, we asses and compare the quantitative consistency of the in-sample and out-of-sample reconstructions to the observed IDR locations using the value of B_z evaluated at the location of the IDR, $B_{z,\mathrm{IDR}} = B_z(\mathbf{r}_{\mathrm{IDR}})$, along with the equatorial distance between the IDR and the $B_z = 0$ nT isocontour, $D_{0\mathrm{nT}}$. Values of $B_{z,\mathrm{IDR}} = 0$ nT and $D_{0\mathrm{nT}} = 0 R_E$ register a perfectly consistent reconstruction. Table 1 reports the values of $B_{z,\mathrm{IDR}}$ for all 26 IDR events, with the first and second columns stating the IDR event name and its location, while the in-sample and out-of-sample $B_{z,\mathrm{IDR}}$ values belong to columns 3 and 4, respectively. The last row displays the median of the absolute value of $B_{z,\mathrm{IDR}}$ across all 26 events.

Of the 26 IDR events, 15 in-sample reconstructions possess a $|B_{z,\mathrm{IDR}}| < 1.5$ nT, while only five of the out-of-sample reconstructions do. Using a larger threshold, the number of IDR event reconstructions with $|B_{z,\mathrm{IDR}}| < 4.0$ nT is 22 and 16 for in-sample versus out-of-sample, respectively. Further, 24 of the 26

Figure 5. Comparison between two in-sample and out-of-sample IDR event reconstructions, Event N and Y, where the resulting B_z equatorial distributions are qualitatively similar to one another. (a) Time series of the SuperMAG storm, $SMRc$, and substorm, SML, indices in black and orange, respectively. The dashed and dotted lines show their smoothed values, $\langle SMRc|$ and $\langle SML|$. The vertical purple line corresponds to the reconstructed time step. (b) The solar wind electric field parameter, vB_z^{IMF}, and the dynamic pressure, P_{dyn}, in black and orange respectively. The dotted black line shows the smoothed parameter $\langle vB_s|$. (c) The equatorial distribution of the z-component of the in-sample reconstructed magnetic field, ignoring deformation effects. The large green dot indicates the location of MMS when it observed an IDR while the small gray dots show the spacecraft record locations contained in the NN subset used to fit the magnetic field architecture, locations are projected to the equatorial (x-y) plane. Panel (d) The same as panel (c) but for the out-of-sample reconstruction. (e) The difference between in-sample and out-of-sample reconstruction.

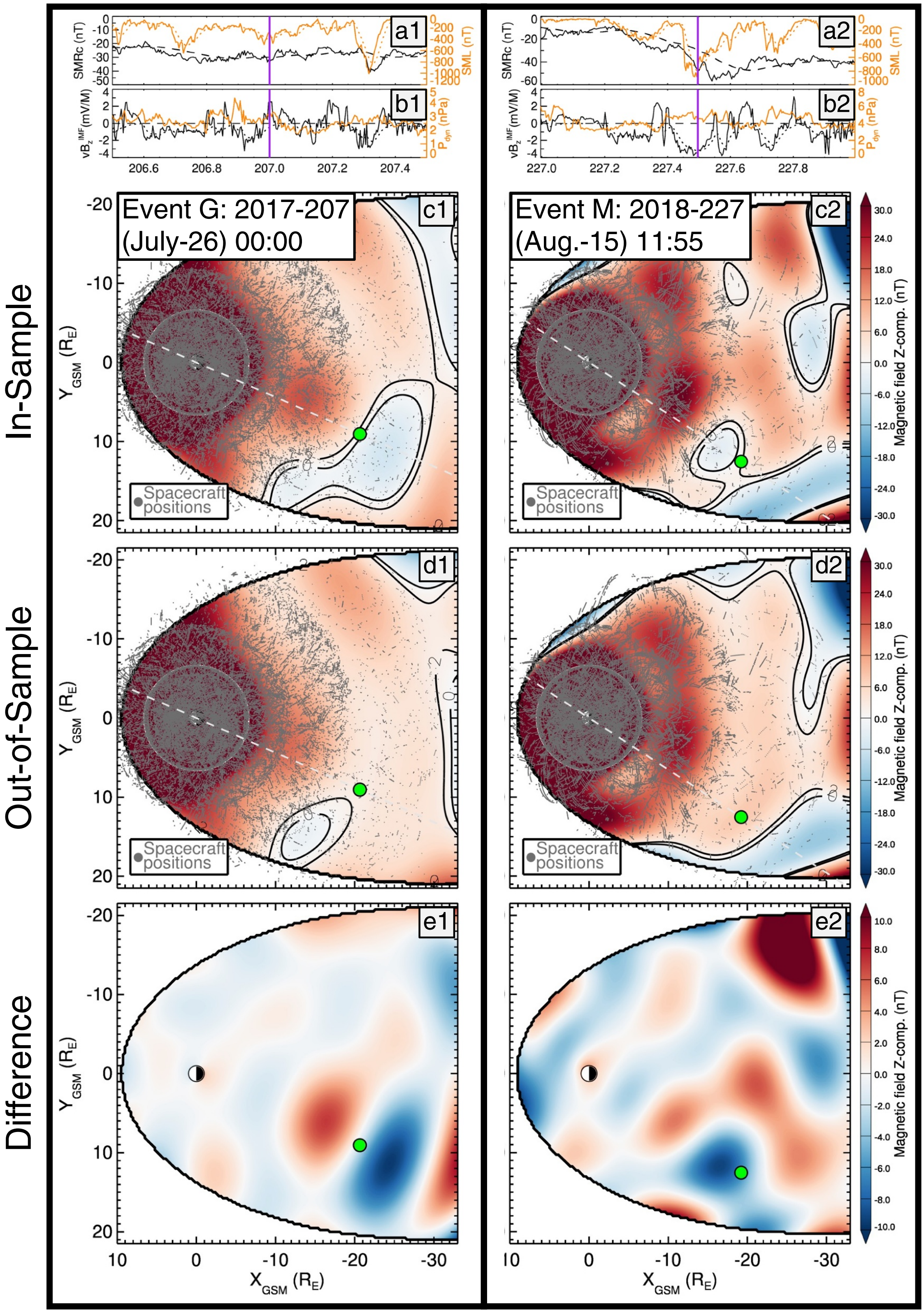

Figure 6. Comparison between two in-sample and out-of-sample IDR event reconstructions, Event G and M, where the resulting B_z equatorial distributions are not qualitatively similar to one another. The descriptions for the panels are the same as Figure 5 but for different events.

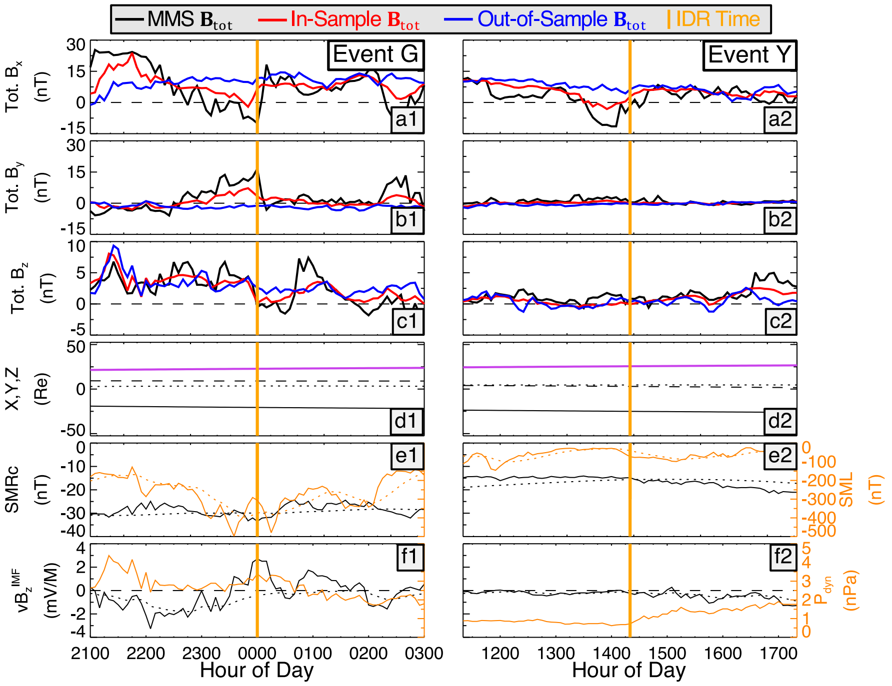

Figure 7. Validating the in-sample and out-of-sample reconstructions of Event G (left panels) and Y (right panels). (a–c) Time series of the components of the MMS1 observed magnetic field averaged to a 5-min cadence (black line) compared to the in-sample (red line) and out-of-sample (blue line) DM-based empirical reconstructions in GSM. The time step when MMS observed an IDR, rounded to the nearest 5-min, is indicated by the yellow vertical line. (d) The x (solid black line), y (dashed black line), z (dotted black line), and radial distance (solid purple line) of the MMS1 ephemeris in GSM. (e) Time series of the SuperMAG storm, *SMRc*, and substorm, *SML*, indices in black and orange, respectively. The dashed and dotted lines show their smoothed values, $\langle SMRc|$ and $\langle SML|$. (f) The solar wind electric field parameter, vB_z^{IMF}, and the dynamic pressure, P_{dyn}, in black and orange respectively. The dotted black line shows the smoothed parameter $\langle vB_s|$.

reconstructions have $|B_{z,\mathrm{IDR}}^{(\mathrm{in})}| < |B_{z,\mathrm{IDR}}^{(\mathrm{out})}|$. This indicates the in-sample magnetometer records do indeed result in more consistent reconstructions, which is also reflected in the median values across all events: 1.1 nT for in-sample compared to 2.9 nT for out-of-sample. However, this comparative analysis does not address the predictive capability of these reconstructions. To assess this, we pose the question, how much more consistent are the reconstructions compared to random chance?

Here, we use skill score, defined as $S = \frac{Metric(model) - Metric(reference)}{Metric(perfect) - Metric(reference)}$ (Liemohn et al., 2021; Murphy, 1988), to quantify the predictive accuracy of the reconstructions. Skill score quantifies a modeled metric's "skill" relative to some reference. A skill score of unity represents a perfect model, while a skill score of zero means the model performs equally as well as the reference. Negative skill scores indicate worse performance relative to the reference.

The reference used to evaluate the skill score is the mean value of $B_{z,\mathrm{IDR}}$ as if the IDR's location were randomly located within the tail. The domain over which the random samples are drawn is limited to $r = [15.7, 29.3]R_E$, where the lower limit corresponds to the radial extent of the IDR nearest to the planet (Event N), while the higher limit is the apogee of the MMS mission and represents the farthest point from which an IDR could have been observed. The domain is also limited to be within the modeled magnetopause boundary for each IDR event reconstruction. Thus, the domain represents the spatial range over which IDRs could have reasonably been observed. For each IDR reconstruction, 5,000 (x, y) coordinates are randomly generated within this domain, and $B_{z,\mathrm{random}}$ for each sample is computed. Their mean values over the 5,000 random samples are reported inside the parentheses in columns 3 and 4 in Table 1. The corresponding Skill Scores, computed as

$$S_{B_z} = \frac{\mathrm{mean}(|B_{z,\mathrm{random}}|) - |B_{z,\mathrm{IDR}}|}{\mathrm{mean}(|B_{z,\mathrm{random}}|)}, \tag{9}$$

Table 2

Consistency Between the Reconstructed Magnetotail Magnetic Field and the IDR Location Observed by MMS

IDR	$D_{0\mathrm{nT}}^{(\mathrm{in})}$ (R_E)	$D_{0\mathrm{nT}}^{(\mathrm{out})}$ (R_E)	$S_{D_0}^{(\mathrm{in})}$	$S_{D_0}^{(\mathrm{out})}$	$D_z^{(\mathrm{in})}$ (R_E)	$D_z^{(\mathrm{out})}$ (R_E)
A	3.5(2.3)	3.9(2.4)	−0.50	−0.63	0.0	−0.0
B	2.1(4.3)	2.6(4.1)	0.51	0.38	0.3	0.4
C	3.8(7.0)	13.8(9.5)	0.46	−0.45	−0.6	−0.7
D	10.0(6.2)	9.3(6.0)	−0.61	−0.54	−0.5	−0.5
E	8.6(16.9)	8.5(16.9)	0.49	0.49	0.4	0.6
F	11.2(6.4)	11.6(9.4)	−0.75	−0.24	−1.2	−1.4
G	0.3(9.1)	5.3(9.8)	0.97	0.45	1.1	1.1
H	2.2(4.5)	5.6(5.1)	0.51	−0.11	0.4	0.8
I	15.4(9.4)	16.3(9.8)	−0.65	−0.67	0.2	0.3
J	8.1(7.9)	8.1(7.8)	−0.02	−0.04	−0.4	−0.4
K	5.2(6.9)	5.2(10.1)	0.25	0.49	−0.1	−0.2
L	5.5(11.6)	3.6(7.5)	0.53	0.52	−0.4	−0.3
M	0.9(3.1)	3.8(4.3)	0.71	0.12	0.6	0.1
N	1.9(6.4)	2.5(6.0)	0.70	0.58	−0.3	−0.3
O	0.1(4.1)	3.1(3.6)	0.97	0.14	0.8	0.4
P	30.4(36.7)	4.4(9.5)	0.17	0.54	−0.5	−0.2
Q	0.6(2.9)	2.5(3.5)	0.78	0.27	0.7	−0.1
R	1.2(3.4)	0.6(3.4)	0.64	0.83	2.8	2.7
S	2.0(13.0)	7.1(11.6)	0.85	0.39	1.4	1.0
T	1.6(4.2)	3.4(4.2)	0.62	0.18	−0.2	−0.1
U	0.6(5.9)	2.3(6.3)	0.90	0.63	−0.4	−0.6
V	1.4(8.1)	1.6(7.9)	0.82	0.80	0.0	0.2
W	1.9(4.2)	1.8(3.6)	0.55	0.50	−0.1	−0.1
X	1.8(2.5)	1.8(2.5)	0.28	0.28	−0.2	−0.0
Y	0.5(10.9)	1.8(11.7)	0.96	0.84	0.4	0.7
Z	12.6(20.4)	13.7(7.1)	0.39	−0.94	0.0	0.2
Med	2.1(6.4)	3.8(6.7)	0.52	0.33	0.0	−0.0

Note. The first column indicates the IDR event, labeled A–Z. The second and third columns indicate the equatorial distance between the location of the MMS observed IDR and the reconstructed $B_z = 0$ nT isocontour for the in-sample and out-of-sample reconstructions, respectively. The values inside the parentheses indicate the mean of these values due to random chance. The fourth and fifth columns display the skill score of the in-sample and out-of-sample reconstructions, respectively, compared to random chance. The sixth and seventh columns display the z-distance between the observed IDR and the location of the neutral sheet for the in-sample and out-of-sample reconstructions, respectively. The last row shows the median of the columns over the 26 events.

are listed in columns 5 and 6 in Table 1 for the in-sample and out-of-sample reconstructions respectively. For the in-sample reconstructions, all but one (Event Z) have skill scores greater than zero, while 21 of the 26 out-of-sample reconstructions possess a positive skill score. The median across all events is $S_{B_z}^{\mathrm{in}} = 0.73$ and $S_{B_z}^{\mathrm{out}} = 0.41$ for the in-sample and out-of-sample reconstructions respectively. While this confirms the in-sample reconstructions are indeed more consistent than the out-of-sample in reproducing a zero B_z at the IDR location, the out-of-sample reconstructions are notably better compared to random chance and are thus somewhat predictive of the location of reconnection in the tail.

Five of the out-of-sample event reconstructions possess a negative skill score (Events A, L, M, Q, and Z), meaning they perform worse than random chance. All five IDRs associated with these events were located quite far away from midnight local time $|y_{\mathrm{IDR}}| > 11R_E$. Other IDR events, such as Event N, O, and P, also have low out-of-sample skill scores (<0.18) and are also located quite far from the meridional plane $y_{\mathrm{IDR}} > 12.5R_E$. Perhaps this indicates that the y location of these particular IDRs is far enough into the tails of the occurrence rate distribution that they cannot be accurately reconstructed using out-of-sample records. For instance, a statistical analysis of tail reconnection events observed by Geotail showed that the occurrence rate dropped precipitously beyond $y = [-8, +14]R_E$ with a peak between $y = [+4, +8]R_E$ (Nagai et al., 2023). However, Event J ($y = 13.0R_E$) and Event R ($y = 12.7R_E$) are likewise located near the tails of this occurrence rate distribution, but have out-of-sample skill scores >0.6.

The second metric used to assess the predictive capability of the reconstructions is the previously described equatorial distance between the $B_z = 0$ nT isocontour and the location of the observed IDR, $D_{0\mathrm{nT}}$. Table 2 reports $D_{0\mathrm{nT}}$ for the in-sample and out-of-sample reconstructions in the first and second columns, respectively. For the in-sample reconstructions, 15 are within $D_{0\mathrm{nT}} \lessapprox 2.1R_E$, which is comparable to the findings of Stephens et al. (2023) which classified 16 events as “hits”, defined as being $D_{0\mathrm{nT}} < 2.0R_E$. In contrast, only five out-of-sample events display such consistency, although 14 are within $D_{0\mathrm{nT}} \lessapprox 4.0R_E$. Overall, 19 in-sample reconstructions possess a smaller value $D_{0\mathrm{nT}}$ than their out-of-sample counterparts, and the median across all events is also smaller, $2.1R_E$ versus $3.8R_E$. Overall, these results confirm that the in-sample magnetometer records yield more consistent reconstructions.

These values are compared against their means, computed over the random sampling described above, and are listed in parentheses in the second and third columns of Table 2, along with their corresponding skill scores in the fourth and fifth columns. Five in-sample and eight out-of-sample reconstructions have a negative skill score, indicating they are less consistent with the observed IDR location compared to random chance. Meanwhile, the median $D_{0\mathrm{nT}}$ skill scores across the 26 events are $S_{D_0}^{(\mathrm{in})} = 0.52$ and $S_{D_0}^{(\mathrm{out})} = 0.33$, which indicates that both the in-sample and out-of-sample reconstructions result in lower equatorial distances between the observed IDR and the $B_z = 0$ nT isocontour than random chance alone would predict.

An alternative way to represent the skill of a metric is by using the mean-square-error (MSE) (Liemohn et al., 2021; Murphy, 1988), in which the equation for skill score becomes:

$$SS = 1 - \frac{MSE_{\text{model}}}{MSE_{\text{reference}}}, \tag{10}$$

where MSE is the sum of the square differences between modeled values and observations divided by the total number of observations. Computing this based on the $B_{z,\text{IDR}}$ metric results in skill scores of $SS_{\text{MSE,B}_z} = 0.72$ and 0.20 for the in-sample and out-of-sample reconstructions respectively, while its value based on $D_{0\text{nT}}$ takes the values of $SS_{\text{MSE,D}_0} = 0.43$ and 0.21 respectively. Note, all four skill scores based on the MSE are lower than their median values computed across the 26 IDR events shown in Tables 1 and 2. This is likely because the MSE-based computation is more susceptible to outliers as it is based on the square of the differences.

5. Bootstrapping Test for Event Y Reconstruction

Bootstrapping quantifies an empirical model's sensitivity to the particular sample of data from which it is constructed (Efron, 1979; Press et al., 1992). When a model is fit to a set of data, that sample is drawn from a much larger population of all hypothetical data representing the system. This inherently introduces sampling error, where the sample is not fully representative of the population from which it is drawn, due to noise or biasing issues. Knowledge of the true sampling error is not possible since the population is unknown; however, bootstrapping introduces a method for estimating the sampling error by randomly resampling the sample. The model can then be fit to this resample of data, termed a bootstrap, and compared to the model fit to the original sample to estimate the sampling error. The bootstrap should contain the same number of records as the original sample, meaning the bootstrap will contain repeated records, termed "sampling with replacement", while other records in the original sample will not be selected for the bootstrap, termed "out-of-bag" records (e.g., Martínez-Muñoz & Suárez, 2010, and references therein). This bootstrapping process can then be repeated many times to quantify the variability, for example, using metrics such as variance and standard deviation, of the model output due to resampling. Note that bootstrapping does not reveal the actual error of the model; that is, it does not measure the difference between the modeled quantity and its true value. Instead, it only estimates the model's sampling error. However, it does provide a means for assessing the model error by comparing the model output to the out-of-bag records. For the sake of brevity, such an out-of-bag analysis will not be conducted here and will be explored in a future study.

Here, the bootstrapping approach is applied to the empirical reconstruction of Event Y (5 August 2020, 14:20). The out-of-sample reconstruction of Event Y, shown in Figure 5, included $S_{\text{NN}} = 101,803$ magnetometer records. These records are resampled with replacement to construct 100 different bootstrap samplings. The SST19 model architecture is then fit to each of these bootstraps using the procedure described in Section 4, using the same set of initial parameters, same weights, and 120 iterations. Figure 8 displays the mean (panel b) and standard deviation (panel d) of the equatorial distribution for the reconstructed external field, B_{ext}, over the 100 bootstraps. The mean of the bootstraps is compared to the original out-of-sample reconstruction (panel a) by plotting the difference between the two in panel c. Overall, the largest differences, $B_z > 1$ nT, appear tailward of Geotail's primary apogee of $r = 31R_E$, where data is very sparse. Inside $31R_E$, the differences are generally small, $|B_z| < 0.5$ nT, except for regions along the duskside magnetopause where there happens to be a lack of data, in which the differences reach $|B_z| \approx 1$ nT. The standard deviation of B_z in the bootstrap reconstructions displays similar patterns, with the highest values, $\sigma B_z > 1$ nT, located tailward of $31R_E$. Earthward of this, $\sigma B_z \lesssim 1$ nT.

The bootstrapping analysis also allows for the investigation of the variability of the 10 free non-linear parameters due to sampling effects. Table 3 shows the mean and standard deviation of the 10 parameters computed over the 100 bootstraps. The twisting parameter, TW, has the largest relative variability $\left(\frac{\sigma_{\text{TW}}}{<TW>} = 0.383\right)$. This parameter dictates the degree of current sheet twisting in the tail (Tsyganenko, 2014), which is correlated with the solar wind B_y^{IMF} (e.g., Cowley, 1981; Sibeck et al., 1985; Zhang et al., 2002). The state space used for the DM procedure (Section 2.1) does not include knowledge of the B_y^{IMF}, therefore, the NN magnetometer records included in the reconstruction will likely include a wide variety of B_y^{IMF} conditions, increasing the variability of TW. Future studies can potentially mitigate this by adding a sixth parameter to the state space, which includes B_y^{IMF}. The parameter with the next largest relative variability is ϵ, with $\frac{\sigma_\epsilon}{<\epsilon>} = 0.114$, while the remaining parameters have a relative variability below 0.1.

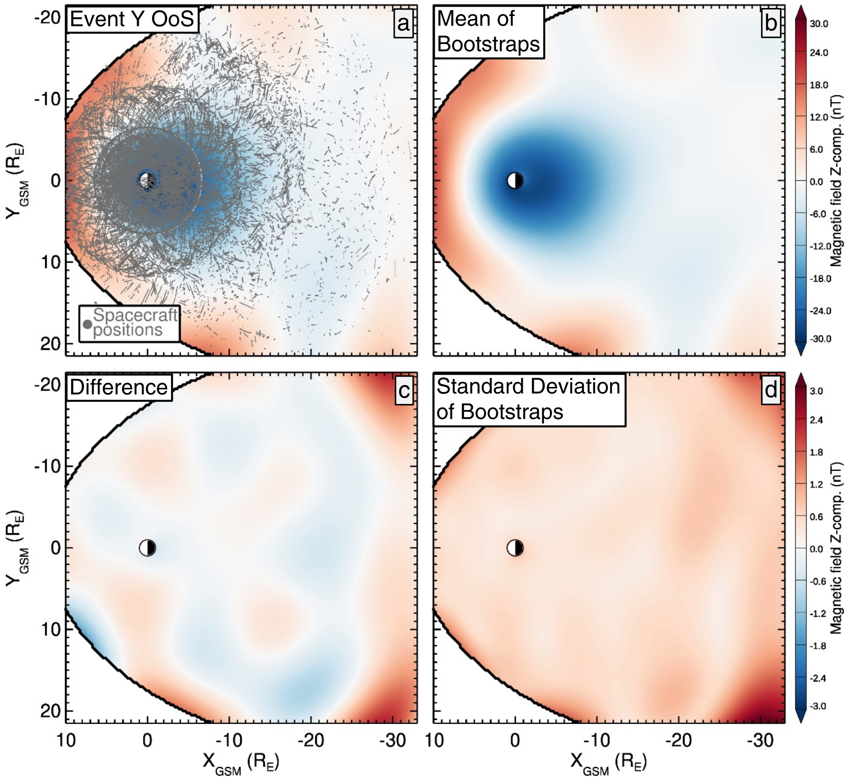

Figure 8. Bootstrapping analysis of Event Y (5 August 2020, 14:20). (a) The equatorial distribution of *z*-component of the out-of-sample reconstructed external magnetic field, $B_{\text{ext},x}$, ignoring deformation effects. The small gray dots show the spacecraft record locations contained in the NN subset used to fit the magnetic field architecture projected to the equatorial (*x*-*y*) plane. Panel (b) The same as panel (a) but now for the mean over the 100 bootstrap (resampled) reconstructions. (c) The difference between the out-of-sample reconstruction and the mean over the 100 bootstrap reconstructions. Panel (d) The same as panel (a) but now for the standard deviation over the 100 bootstrap reconstructions.

6. Discussion and Conclusions

In this study, we aim to further explore, validate, and quantify the fidelity of SST19 reconstructions of the magnetospheric magnetic field during 26 magnetotail reconnection events (labeled A–Z) observed by MMS (Rogers et al., 2019, 2023) as previously studied by Stephens et al. (2023). SST19 reconstructs the global storm and substorm configuration of the magnetospheric magnetic field at a given time step by mining a multi-decade, multi-spacecraft archive of space magnetometer data for a small subset of records from other times when the magnetosphere was in a similar dynamical state (Section 2.1) and then uses that data to fit a flexible analytical architecture (Section 2.2) used to describe the primary magnetospheric current systems. We have explored three different aspects of the SST19 tail reconstructions:

First, in Section 3, we fit the SST19 model architecture by sampling prescribed magnetic field distributions that contain magnetotail X- and O-lines. These distributions are constructed by inserting a disk current system (Tsyganenko & Peredo, 1994) into the magnetotail of the T96 empirical magnetic field model (Tsyganenko, 1995, 1996). This was repeated 100 times by constructing disks of random sizes and at random locations within the magnetotail. These distributions were sampled at a set of spacecraft locations determined using the k-Nearest Neighbor data mining procedure described in Section 2.1.1, thereby mimicking a realistic distribution of samples used in the actual magnetic field reconstructions. This investigation revealed several findings. First, it demonstrated that smaller X- and O-lines were generally not resolved using the SST19 architecture, while the majority of the larger ones were successfully reconstructed. Although there was no precise disk size demarcating the two regimes, generally disks of radius $\gtrsim 3.5R_E$ were successfully reconstructed while those $\lesssim 2.5R_E$ were not. Presumably, using a larger number of equatorial expansions in SST19's description of the equatorial currents, determined by the values (M, N) in Equation 5, would help resolve these smaller X- and O-lines, but this hazards overfitting. However, a natural extension of this exercise can be used in future SST19 versions as a more rigorous

Table 3

Bootstrapping Analysis Non-Linear Parameters Describing SST19's Architecture (Section 2.2.) for the Reconstruction of Event Y

Parameter	OoS value	Bootstrap mean	Bootstrap σ	Bootstrap $\frac{\sigma}{mean}$
D	3.68	3.84	0.25	0.065
D_0	4.30	4.57	0.35	0.076
α	2.19	2.27	0.09	0.039
β	0.0321	0.0317	0.0021	0.068
ϵ	0.11	0.11	0.01	0.114
R_H	7.62	7.69	0.23	0.029
G	2.27	2.32	0.15	0.062
TW	1.43×10^{-3}	1.51×10^{-3}	0.58×10^{-3}	0.383
κ_{R1}	0.606	0.603	0.032	0.053
κ_{R2}	0.912	0.852	0.036	0.043

Note. The first column lists the parameter while the second column states its fit value using the out-of-sample set of NNs (Section 4). The third and fourth columns list the mean and standard deviation of these parameters after fitting SST19 to the 100 bootstraps (resamples). The fifth column displays the relative variability of the parameter, defined as the ratio of its standard deviation to its mean.

means of selecting the optimal value of (M, N) given a set value of k_{NN}. For example, two different spacecraft distributions can be used, one for fitting and one for validation. As the number of expansions increases, that is, by using increasingly larger values for (M, N), the root-mean-square (RMS) differences will decrease for both the fitting and validation sets. However, at some value of (M, N), the validation set RMS differences will reach a minimum. Increasing the number of expansions beyond this will result in overfitting, thereby increasing the validation set RMS differences. Thus, sampling prescribed distributions may provide a means of tuning the hyperparameters describing SST19's architecture in an approach similar to model cross-validation. However, such an approach is not straightforward as the optimal value of (M, N) likely varies spatially due to the inhomogeneity of in situ spacecraft observations, meaning one spatial region may be underfit while another region is simultaneously overfit. A potential workaround is the approach employed by Stephens and Sitnov (2021), in which different equatorial model resolutions are effectively merged. It should be noted that the benchmarking performed in Section 3 only tests the SST19 model architecture and not the kNN data mining (DM) method. For example, in each of the 100 randomized tests, the samples used to benchmark the architecture are drawn from a single prescribed magnetic field distribution, whereas in the actual SST19 algorithm, they are drawn from different, although presumably similar, distributions. This necessitates the additional analyses performed in this study that affirmatively test aspects of the DM method. The entire SST19 algorithm, including its DM portion, could be benchmarked by simulating the magnetospheric magnetic field using global magnetohydrodynamics-based models (e.g., Sorathia et al., 2020), and replacing the observed space magnetometer records (Section 2.1.2) and observed geomagnetic indices with their simulated values. However, such an approach would be computationally infeasible as the archive spans nearly three decades. Furthermore, these simulations may need to be tuned to yield realistic magnetotail reconnection configurations (Arnold et al., 2023).

In Section 4, we repeat the primary investigation of Stephens et al. (2023) and now perform both in-sample (using data from the event) and out-of-sample (excluding data from the event) reconstructions. In particular, the out-of-sample reconstructions reveal the predictive nature of the SST19 algorithm. The original study characterized the consistency between the reconstructed magnetic field and the MMS observed reconnection location using a “hit” analysis based on the distance to the reconstructed $B_z = 0$ nT isocontour, $D_{0\mathrm{nT}}$. Here, we continue to employ $D_{0\mathrm{nT}}$ but also use the value of the reconstructed field at the observed reconnection location, $B_{z,\mathrm{IDR}}$, as consistency metrics, both of which have an ideal value of zero. The median value for $|B_{z,\mathrm{IDR}}|$ across the 26 event reconstructions was 1.1 and 2.9 nT for the in-sample and out-of-sample respectively, while it was 2.1 and 3.8R_E for $D_{0\mathrm{nT}}$ respectively. This indicates that the in-sample data records improve the consistency of the reconstructions. However, an important element missing from the original analysis was a reference to compare the consistency between SST19 and the MMS observations. We have addressed that here by evaluating the skill scores of $D_{0\mathrm{nT}}$ and $B_{z,\mathrm{IDR}}$ referenced against random chance (Tables 2 and 3), that is, these skill scores quantify the degree to which the reconstructions are better at resolving the reconnection location compared to random chance: a skill score of one represents perfect consistency, zero is equivalent to random chance, and a negative score means it performs worse than random chance. Combining both metrics, $D_{0\mathrm{nT}}$ and $B_{z,\mathrm{IDR}}$, 88% (46 of 52) of the in-sample reconstructions possess a positive skill score while 75% (39 of 52) of the out-of-sample reconstructions do. The median skill scores across the events for $|B_{z,\mathrm{IDR}}|$ are 0.73 and 0.41 for the in-sample and out-of-sample reconstructions, respectively, while they are 0.52 and 0.33 for $D_{0\mathrm{nT}}$, respectively. Therefore, although the in-sample reconstructions have generally higher skill scores, the out-of-sample reconstructions indeed predict the reconnection location better than random chance. However, it is not known whether this method provides more knowledge about the reconnection site than empirically derived occurrence rate models (Genestreti et al., 2013, 2014). This could be tested by replacing the uniform distribution used to draw the random samples when computing the skill score with a distribution function based on the occurrence rate model.

The last Section 5 performed a bootstrapping analysis on the SST19 reconstruction of Event Y (5 August 2020, 14:20). Bootstrapping is a technique used to estimate an empirical model's variability due to sampling. Here, we constructed 100 bootstraps and computed the mean and standard deviations for the resulting magnetic field distributions and SST19's free non-linear parameters. Overall, the magnetic field distribution was robust during resampling, with differences and standard deviations being <1 nT across most of the modeling domain (Figure 8). Likewise, the majority of the non-linear parameters were also robust during resampling with relative variabilities near or below 10% (Table 3), the exception being the twist parameter TW. This finding motivates incorporating B_y^{IMF} into the kNN data mining procedure perhaps as a sixth state parameter. It should be noted that this bootstrapping analysis was only performed for a single time step, and it is unclear whether the results are generalizable to all times. For instance, there may be reconstructions where one or more outlier magnetometer records significantly alter the magnetic field distribution, and as such, additional bootstrapping tests should be conducted in future studies.

The quantitative analysis performed here provides a framework for future versions of the DM algorithm to be validated, improved, and optimized, allowing for the pursuit of additional questions. The limited number (26) of MMS-observed tail reconnection events hampers the statistical robustness of this study. However, a recent survey of Geotail magnetic field and plasma data identified a much larger set (246) of tail reconnection events (Nagai et al., 2023). Further, the current magnetometer archive is ripe for expansion. For instance, the Geotail portion of the archive includes no data after 2005, thereby it is missing approximately 17 years of data which would populate the mid-tail region out to $r = 31R_E$. Likewise, the THEMIS and Cluster portions of the archive do not include data after 2015, whose inclusion would populate the archive with additional data in the near-tail region out to $r = 12$ and $19R_E$, respectively. Such an investigation could address several questions: How consistent is the DM approach at resolving Geotail-observed reconnection events? What is the capacity of the DM approach in predicting the location of reconnection for an independent spacecraft mission? For instance, can Geotail data be used to predict where MMS will observe reconnection, and vice versa? Furthermore, the approach used here can be used to improve and optimize future versions of the algorithm. For instance, does incorporating the local-time SuperMAG indices, which proved crucial for the discovery of the so-called “dawnside current wedge” during storms (Ohtani et al., 2018, 2023; Sorathia et al., 2023), improve the skill score? Incorporating other effects could also increase the skill score, and thereby the predictive capacity of future DM algorithms. For example, the magnetotail twisting effect may be resolved by adding the B_y^{IMF} to the DM procedure, and the windsock effect may be captured by switching to Geocentric Solar Wind (GSW) coordinates (e.g., Sergeev et al., 2008). In conclusion, the study presented here has demonstrated that the application of data mining techniques to historical sets of sparse observations is feasible and can resolve repeatable dynamical features of the magnetosphere, including the location of magnetotail reconnection. However, many questions and avenues for improvement remain open.

Conflict of Interest

The authors declare no conflicts of interest relevant to this study.

Data Availability Statement

The digital results of this study, including the sets of identified nearest neighbors and their associated weights, the fit set of amplitude coefficients and non-linear parameters for the SST19 architecture, model output data, and data used for the figures, have been included in a Zenodo archive (Stephens et al., 2025). This Zenodo archive also consists of the input datasets: (a) the magnetometer archive, a mirror of that available on the SPDF website (Korth et al., 2018), but extended to include MMS magnetometer data (Russell et al., 2022a, 2022b, 2022c, 2022d); (b) the 5-min OMNI dataset (Papitashvili & King, 2020) used for describing solar wind conditions; and (c) the 1-min SMR and SML indices were acquired from the SuperMAG web page (https://supermag.jhuapl.edu/indices/). This Zenodo archive also includes the FORTRAN implementation of the SST19 model, a mirror of that available on the ARGUS GitHub page (https://github.com/grantkstephens/ARGUS).

Acknowledgments

The authors acknowledge the various spacecraft missions and instrument teams whose data were used in this study, including Geotail, Polar, IMP 8, Cluster, THEMIS, Van Allen Probes, MMS, and GOES data obtained via NSSDC CDAWeb online facility, as well as Wind, ACE, and DSCOVR solar wind/IMF data that went into the production of the OMNI data obtained via NASA/GSFC's Space Physics Data Facility's OMNIWeb service (Papitashvili & King, 2020). We acknowledge the substorm timing list identified by the SOPHIE technique (Forsyth et al., 2015), the SMU and SML indices (Newell & Gjerloev, 2011); and the SuperMAG collaboration (Gjerloev, 2012). The work on this paper for MIS and GKS also benefited greatly from the discussions at the ISSI workshops, "Magnetotail Dipolarizations: Archimedes Force or Ideal Collapse?" and "Imaging the invisible: Unveiling the global structure of Earth's dynamic magnetosphere", held in May 2022 and May 2023. This work was funded by NASA Grants 80NSSC24K0556 and 80NSSC20K1787, along with JHU/APL's Part-Time Study Program's doctoral dissertation leave.

References

Alken, P., Thébault, E., Beggan, C. D., Amit, H., Aubert, J., Baerenzung, J., et al. (2021). International geomagnetic reference field: The thirteenth generation. *Earth Planets and Space*, *73*(1), 49. https://doi.org/10.1186/s40623-020-01288-x

Angelopoulos, V., Artemyev, A., Phan, T. D., & Miyashita, Y. (2020). Near-Earth magnetotail reconnection powers space storms. *Nature Physics*, *16*(3), 317–321. https://doi.org/10.1038/s41567-019-0749-4

Anguita, D., Ghio, A., Oneto, L., & Ridella, S. (2012). In-sample and out-of-sample model selection and error estimation for support vector machines. *IEEE Transactions on Neural Networks and Learning Systems*, *23*(9), 1390–1406. https://doi.org/10.1109/tnnls.2012.2202401

Arnold, H., Sorathia, K., Stephens, G. K., Sitnov, M. I., Merkin, V. G., & Birn, J. (2023). Data mining inspired localized resistivity in global MHD simulations of the magnetosphere. *Journal of Geophysical Research: Space Physics*, *128*(2), e2022JA030990. https://doi.org/10.1029/2022ja030990

Artemyev, A., & Zelenyi, L. (2012). Kinetic structure of current sheets in the earth magnetotail. In *Microphysics of cosmic plasmas* (pp. 343–364). Springer. US. https://doi.org/10.1007/978-1-4899-7413-6_13

Auster, H. U., Glassmeier, K. H., Magnes, W., Aydogar, O., Baumjohann, W., Constantinescu, D., et al. (2008). The Themis fluxgate magnetometer. *Space Science Reviews*, *141*(1–4), 235–264. https://doi.org/10.1007/s11214-008-9365-9

Baker, D. N., Pulkkinen, T. I., Angelopoulos, V., Baumjohann, W., & McPherron, R. L. (1996). Neutral line model of substorms: Past results and present view. *Journal of Geophysical Research*, *101*(A6), 12975–13010. https://doi.org/10.1029/95JA03753

Balogh, A., Carr, C. M., Acuña, M. H., Dunlop, M. W., Beek, T. J., Brown, P., et al. (2001). The cluster magnetic field investigation: Overview of in-flight performance and initial results. *Annales Geophysicae*, *19*(10/12), 1207–1217. https://doi.org/10.5194/angeo-19-1207-2001

Borovsky, J. E. (2008). The rudiments of a theory of solar wind/magnetosphere coupling derived from first principles. *Journal of Geophysical Research*, *113*(A8). https://doi.org/10.1029/2007ja012646

Cassak, P. A., & Shay, M. A. (2007). Scaling of asymmetric magnetic reconnection: General theory and collisional simulations. *Physics of Plasmas*, *14*(10), 102114. https://doi.org/10.1063/1.2795630

Cowley, S. (1981). Magnetospheric asymmetries associated with the y-component of the IMF. *Planetary and Space Science*, *29*(1), 79–96. https://doi.org/10.1016/0032-0633(81)90141-0

Dungey, J. W. (1953). Conditions for the occurrence of electrical discharges in astrophysical systems. *The London, Edinburgh and Dublin Philosophical Magazine and Journal of Science*, *44*(354), 725–738. https://doi.org/10.1080/14786440708521050

Dungey, J. W. (1961). Interplanetary magnetic field and the auroral zones. *Physical Review Letters*, *6*(2), 47–48. https://doi.org/10.1103/PhysRevLett.6.47

Eastwood, J. P., Phan, T., Mozer, F. S., Shay, M. A., Fujimoto, M., Retinò, A., et al. (2007). Multi-point observations of the hall electromagnetic field and secondary island formation during magnetic reconnection. *Journal of Geophysical Research*, *112*(A6). https://doi.org/10.1029/2006ja012158

Eastwood, J. P., Phan, T. D., Øieroset, M., & Shay, M. A. (2010). Average properties of the magnetic reconnection ion diffusion region in the earth's magnetotail: The 2001–2005 cluster observations and comparison with simulations. *Journal of Geophysical Research*, *115*(A8). https://doi.org/10.1029/2009ja014962

Efron, B. (1979). Bootstrap methods: Another look at the jackknife. *Annals of Statistics*, *7*(1). https://doi.org/10.1214/aos/1176344552

Farrugia, C. J., Rogers, A. J., Torbert, R. B., Genestreti, K. J., Nakamura, T. K. M., Lavraud, B., et al. (2021). An encounter with the ion and electron diffusion regions at a flapping and twisted tail current sheet. *Journal of Geophysical Research: Space Physics*, *126*(3), e2020JA028903. https://doi.org/10.1029/2020ja028903

Forsyth, C., Rae, I. J., Coxon, J. C., Freeman, M. P., Jackman, C. M., Gjerloev, J., & Fazakerley, A. N. (2015). A new technique for determining substorm onsets and phases from indices of the electrojet (SOPHIE). *Journal of Geophysical Research: Space Physics*, *120*(12). https://doi.org/10.1002/2015ja021343

Fukao, S., Ugai, M., & Tsuda, T. (1975). Topological study of magnetic field near a neutral point. *Report of Ionosphere and Space Research in Japan*, *29*(3), 133–139.

Genestreti, K. J., Fuselier, S. A., Goldstein, J., & Nagai, T. (2013). An empirical model for the location and occurrence rate of near-earth magnetotail reconnection. *Journal of Geophysical Research: Space Physics*, *118*(10), 6389–6396. https://doi.org/10.1002/2013ja019125

Genestreti, K. J., Fuselier, S. A., Goldstein, J., Nagai, T., & Eastwood, J. (2014). The location and rate of occurrence of near-earth magnetotail reconnection as observed by cluster and geotail. *Journal of Atmospheric and Solar-Terrestrial Physics*, *121*, 98–109. https://doi.org/10.1016/j.jastp.2014.10.005

Gjerloev, J. W. (2012). The supermag data processing technique. *Journal of Geophysical Research*, *117*(A9). https://doi.org/10.1029/2012JA017683

Goldstein, H., & Safko, J. (2002). *Classical mechanics*. (3rd ed). Addison Wesley.

Gonzalez, W. D., Joselyn, J. A., Kamide, Y., Kroehl, H. W., Rostoker, G., Tsurutani, B. T., & Vasyliunas, V. M. (1994). What is a geomagnetic storm? *Journal of Geophysical Research*, *99*(A4), 5771–5792. https://doi.org/10.1029/93ja02867

Hesse, M., & Cassak, P. A. (2020). Magnetic reconnection in the space sciences: Past, present, and future. *Journal of Geophysical Research: Space Physics*, *125*(2), e2018JA025935. https://doi.org/10.1029/2018ja025935

Hones, E., Jr. (1979). Transient phenomena in the magnetotail and their relation to substorms. *Space Science Reviews*, *23*(3), 393–410. https://doi.org/10.1007/bf00172247

Hones, E. W., Jr. (1984). Plasma sheet behavior during substorms. In *Magnetic reconnection in space and laboratory plasmas* (pp. 178–184). American Geophysical Union (AGU). https://doi.org/10.1029/GM030p0178

Jackson, D. D. (1972). Interpretation of inaccurate, insufficient and inconsistent data. *Geophysical Journal International*, *28*(2), 97–109. https://doi.org/10.1111/j.1365-246X.1972.tb06115.x

Kletzing, C. A., Kurth, W. S., Acuna, M., MacDowall, R. J., Torbert, R. B., Averkamp, T., et al. (2013). The electric and magnetic field instrument suite and integrated science (EMFISIS) on RBSP. *Space Science Reviews*, *179*(1–4), 127–181. https://doi.org/10.1007/s11214-013-9993-6

Kokubun, S., Yamamoto, T., Acuña, M. H., Hayashi, K., Shiokawa, K., & Kawano, H. (1994). The geotail magnetic field experiment. *Journal of Geomagnetism and Geoelectricity*, *46*(1), 7–21. https://doi.org/10.5636/jgg.46.7

Korth, H., Sitnov, M. I., & Stephens, G. K. (2018). Magnetic field modeling database description final [Dataset]. *NASA Space Physics Data Facility*. Retrieved from https://spdf.gsfc.nasa.gov/pub/data/aaa_special-purpose-datasets/empirical-magnetic-field-modeling-database-with-TS07D-coefficients/

Liemohn, M. W., McCollough, J. P., Jordanova, V. K., Ngwira, C. M., Morley, S. K., Cid, C., et al. (2018). Model evaluation guidelines for geomagnetic index predictions. *Space Weather*, *16*(12), 2079–2102. https://doi.org/10.1029/2018SW002067

Liemohn, M. W., Shane, A. D., Azari, A. R., Petersen, A. K., Swiger, B. M., & Mukhopadhyay, A. (2021). RMSE is not enough: Guidelines to robust data-model comparisons for magnetospheric physics. *Journal of Atmospheric and Solar-Terrestrial Physics*, *218*, 105624. https://doi.org/10.1016/j.jastp.2021.105624

Martínez-Muñoz, G., & Suárez, A. (2010). Out-of-bag estimation of the optimal sample size in bagging. *Pattern Recognition*, *43*(1), 143–152. https://doi.org/10.1016/j.patcog.2009.05.010

McPherron, R. L., Russell, C. T., Kivelson, M. G., & Coleman Jr, P. J. (1973). Substorms in space: The correlation between ground and satellite observations of the magnetic field. *Radio Science*, *8*(11), 1059–1076. https://doi.org/10.1029/RS008i011p01059

McPherron, R. L. (2016). Where and when does reconnection occur in the tail? *Journal of Geophysical Research: Space Physics*, *121*(5), 4607–4610. https://doi.org/10.1002/2015JA022258

McPherron, R. L., Russell, C. T., & Aubry, M. P. (1973). Satellite studies of magnetospheric substorms on August 15, 1968: 9. phenomenological model for substorms. *Journal of Geophysical Research*, *78*(16), 3131–3149. https://doi.org/10.1029/ja078i016p03131

Mead, G. D., & Fairfield, D. H. (1975). A quantitative magnetospheric model derived from spacecraft magnetometer data. *Journal of Geophysical Research (1896-1977)*, *80*(4), 523–534. https://doi.org/10.1029/JA080i004p00523

Menvielle, M., Iyemori, T., Marchaudon, A., & Nosé, M. (2010). Geomagnetic indices. In *Geomagnetic observations and models* (pp. 183–228). Springer. https://doi.org/10.1007/978-90-481-9858-0_8

Miyashita, Y., Miyoshi, Y., Matsumoto, Y., Ieda, A., Kamide, Y., Nosé, M., et al. (2005). Geotail observations of signatures in the near-earth magnetotail for the extremely intense substorms of the 30 October 2003 storm. *Journal of Geophysical Research*, *110*(A9). https://doi.org/10.1029/2005ja011070

Motoba, T., Sitnov, M. I., Stephens, G. K., & Gershman, D. J. (2022). A new perspective on magnetotail electron and ion divergent flows: Mms observations. *Journal of Geophysical Research: Space Physics*, *127*(10), e2022JA030514. https://doi.org/10.1029/2022ja030514

Murphy, A. H. (1988). Skill scores based on the mean square error and their relationships to the correlation coefficient. *Monthly Weather Review*, *116*(12), 2417–2424. https://doi.org/10.1175/1520-0493(1988)116⟨2417:ssbotm⟩2.0.co;2

Nagai, T., Fujimoto, M., Nakamura, R., Baumjohann, W., Ieda, A., Shinohara, I., et al. (2005). Solar wind control of the radial distance of the magnetic reconnection site in the magnetotail. *Journal of Geophysical Research*, *110*(A9). https://doi.org/10.1029/2005JA011207

Nagai, T., Fujimoto, M., Saito, Y., Machida, S., Terasawa, T., Nakamura, R., et al. (1998). Structure and dynamics of magnetic reconnection for substorm onsets with geotail observations. *Journal of Geophysical Research*, *103*(A3), 4419–4440. https://doi.org/10.1029/97ja02190

Nagai, T., & Shinohara, I. (2021). Dawn-dusk confinement of magnetic reconnection site in the near-earth magnetotail and its implication for dipolarization and substorm current system. *Journal of Geophysical Research: Space Physics*, *126*(11), e2021JA029691. https://doi.org/10.1029/2021ja029691

Nagai, T., Shinohara, I., Saito, Y., Ieda, A., & Nakamura, R. (2023). Location and timing of magnetic reconnections in earth's magnetotail: Accomplishments of the 29-year geotail near-earth magnetotail survey. *Journal of Geophysical Research: Space Physics*, *128*(12), e2023JA032023. https://doi.org/10.1029/2023ja032023

Nelder, J. A., & Mead, R. (1965). A Simplex method for function minimization. *The Computer Journal*, *7*(4), 308–313. https://doi.org/10.1093/comjnl/7.4.308

Newell, P. T., & Gjerloev, J. W. (2011). Evaluation of supermag auroral electrojet indices as indicators of substorms and auroral power. *Journal of Geophysical Research*, *116*(A12). https://doi.org/10.1029/2011ja016779

Newell, P. T., & Gjerloev, J. W. (2012). Supermag-based partial ring current indices. *Journal of Geophysical Research*, *117*(A5). https://doi.org/10.1029/2012JA017586

Newell, P. T., Sotirelis, T., Liou, K., Meng, C.-I., & Rich, F. J. (2007). A nearly universal solar wind-magnetosphere coupling function inferred from 10 magnetospheric state variables. *Journal of Geophysical Research*, *112*(A1). https://doi.org/10.1029/2006JA012015

Ohtani, S., Gjerloev, J. W., Anderson, B. J., Kataoka, R., Troshichev, O., & Watari, S. (2018). Dawnside wedge current system formed during intense geomagnetic storms. *Journal of Geophysical Research: Space Physics*, *123*(11), 9093–9109. https://doi.org/10.1029/2018ja025678

Ohtani, S., Sorathia, K., Merkin, V. G., Frey, H. U., & Gjerloev, J. W. (2023). External and internal causes of the stormtime intensification of the dawnside westward auroral electrojet. *Journal of Geophysical Research: Space Physics*, *128*(10), e2023JA031457. https://doi.org/10.1029/2023ja031457

Papitashvili, N. E., & King, J. H. (2020). Omni 5-min data [Dataset]. *NASA Space Physics Data Facility*. https://doi.org/10.48322/gbpg-5r77

Partamies, N., Juusola, L., Tanskanen, E., & Kauristie, K. (2013). Statistical properties of substorms during different storm and solar cycle phases. *Annales Geophysicae*, *31*(2), 349–358. https://doi.org/10.5194/angeo-31-349-2013

Press, W. H., Teukolsky, S. A., Vetterling, W. T., & Flannery, B. P. (1992). *Numerical recipes in c (2nd ed.): The art of scientific computing*. Cambridge University Press.

Rogers, A. J., Farrugia, C. J., & Torbert, R. B. (2019). Numerical algorithm for detecting ion diffusion regions in the geomagnetic tail with applications to mms tail season 1 may to 30 September 2017. *Journal of Geophysical Research: Space Physics*, *124*(8), 6487–6503. https://doi.org/10.1029/2018ja026429

Rogers, A. J., Farrugia, C. J., Torbert, R. B., & Rogers, T. J. (2023). Applying magnetic curvature to mms data to identify thin current sheets relative to tail reconnection. *Journal of Geophysical Research: Space Physics*, *128*(1), e2022JA030577. https://doi.org/10.1029/2022ja030577

Russell, C. T., Anderson, B. J., Baumjohann, W., Bromund, K. R., Dearborn, D., Fischer, D., et al. (2016). The magnetospheric multiscale magnetometers. *Space Science Reviews*, *199*(1–4), 189–256. https://doi.org/10.1007/s11214-014-0057-3

Russell, C. T., Magnes, W., Wei, H., Bromund, K. R., Plaschke, F., Fischer, D., et al. (2022a). Mms 1 flux gate magnetometer (FGM) dc magnetic field, level 2 (l2), survey mode, 8 or 16 sample/s, v4/5 data [Dataset]. *NASA Space Physics Data Facility*. https://doi.org/10.48322/MXBX-R466

Russell, C. T., Magnes, W., Wei, H., Bromund, K. R., Plaschke, F., Fischer, D., et al. (2022b). Mms 2 flux gate magnetometer (FGM) dc magnetic field, level 2 (l2), survey mode, 8 or 16 sample/s, v4/5 data [Dataset]. *Laboratory for Atmospheric and Space Physics; Space Physics Data Facility*. https://doi.org/10.48322/XZ3N-G079

Russell, C. T., Magnes, W., Wei, H., Bromund, K. R., Plaschke, F., Fischer, D., et al. (2022c). Mms 3 flux gate magnetometer (FGM) dc magnetic field, level 2 (l2), survey mode, 8 or 16 sample/s, v4/5 data [Dataset]. *Laboratory for Atmospheric and Space Physics; Space Physics Data Facility*. https://doi.org/10.48322/8S4Y-EN47

Russell, C. T., Magnes, W., Wei, H., Bromund, K. R., Plaschke, F., Fischer, D., et al. (2022d). Mms 4 flux gate magnetometer (FGM) dc magnetic field, level 2 (l2), survey mode, 8 or 16 sample/s, v4/5 data [Dataset]. *Laboratory for Atmospheric and Space Physics; Space Physics Data Facility*. https://doi.org/10.48322/50P5-D131

Russell, C. T., Snare, R. C., Means, J. D., Pierce, D., Dearborn, D., Larson, M., et al. (1995). The GGS/POLAR magnetic fields investigation. *Space Science Reviews*, *71*(1–4), 563–582. https://doi.org/10.1007/bf00751341

Schroeder, J. M., Egedal, J., Cozzani, G., Khotyaintsev, Y. V., Daughton, W., Denton, R. E., & Burch, J. L. (2022). 2d reconstruction of magnetotail electron diffusion region measured by mms. *Geophysical Research Letters*, *49*(19), e2022GL100384. https://doi.org/10.1029/2022gl100384

Sciola, A., Merkin, V. G., Sorathia, K., Gkioulidou, M., Bao, S., Toffoletto, F., et al. (2023). The contribution of plasma sheet bubbles to stormtime ring current buildup and evolution of its energy composition. *Journal of Geophysical Research: Space Physics*, *128*(11), e2023JA031693. https://doi.org/10.1029/2023ja031693

Sergeev, V. A., Tsyganenko, N. A., & Angelopoulos, V. (2008). Dynamical response of the magnetotail to changes of the solar wind direction: An MHD modeling perspective. *Annales Geophysicae*, *26*(8), 2395–2402. https://doi.org/10.5194/angeo-26-2395-2008

Shay, M. A., Drake, J. F., Denton, R. E., & Biskamp, D. (1998). Structure of the dissipation region during collisionless magnetic reconnection. *Journal of Geophysical Research*, *103*(A5), 9165–9176. https://doi.org/10.1029/97ja03528

Shi, X., Stephens, G. K., Artemyev, A. V., Sitnov, M. I., & Angelopoulos, V. (2024). Picturing global substorm dynamics in the magnetotail using low-altitude ELFIN measurements and data mining-based magnetic field reconstructions. *Space Weather*, *22*(10), e2024SW004062. https://doi.org/10.1029/2024sw004062

Shue, J.-H., Song, P., Russell, C. T., Steinberg, J. T., Chao, J. K., Zastenker, G., et al. (1998). Magnetopause location under extreme solar wind conditions. *Journal of Geophysical Research*, *103*(A8), 17691–17700. https://doi.org/10.1029/98JA01103

Sibeck, D. G., Siscoe, G. L., Slavin, J. A., Smith, E. J., Tsurutani, B. T., & Lepping, R. P. (1985). The distant magnetotail's response to a strong interplanetary magnetic field by: Twisting, flattening, and field line bending. *Journal of Geophysical Research*, *90*(A5), 4011–4019. https://doi.org/10.1029/ja090ia05p04011

Singer, H., Matheson, L., Grubb, R., Newman, A., & Bouwer, D. (1996). Monitoring space weather with the GOES magnetometers. In E. R. Washwell (Ed.), *Goes-8 and beyond* (Vol. 2812, pp. 299–308). https://doi.org/10.1117/12.254077

Sitnov, M. I., & Arnold, H. (2022). Equilibrium kinetic theory of weakly anisotropic embedded thin current sheets. *Journal of Geophysical Research: Space Physics*, *127*(11), e2022JA030945. https://doi.org/10.1029/2022ja030945

Sitnov, M. I., Birn, J., Ferdousi, B., Gordeev, E., Khotyaintsev, Y., Merkin, V., et al. (2019). Explosive magnetotail activity. *Space Science Reviews*, *215*(4), 31. https://doi.org/10.1007/s11214-019-0599-5

Sitnov, M. I., & Schindler, K. (2010). Tearing stability of a multiscale magnetotail current sheet. *Geophysical Research Letters*, *37*(8). https://doi.org/10.1029/2010gl042961

Sitnov, M. I., Stephens, G. K., Motoba, T., & Swisdak, M. (2021). Data mining reconstruction of magnetotail reconnection and implications for its first-principle modeling. *Frontiers in Physics*, *9*, 644884. https://doi.org/10.3389/fphy.2021.644884

Sitnov, M. I., Stephens, G. K., Tsyganenko, N. A., Korth, H., Roelof, E. C., Brandt, P. C., et al. (2020). Reconstruction of extreme geomagnetic storms: Breaking the data paucity curse. *Space Weather*, *18*(10), e2020SW002561. https://doi.org/10.1029/2020sw002561

Sitnov, M. I., Stephens, G. K., Tsyganenko, N. A., Miyashita, Y., Merkin, V. G., Motoba, T., et al. (2019). Signatures of nonideal plasma evolution during substorms obtained by mining multimission magnetometer data. *Journal of Geophysical Research: Space Physics*, *124*(11), 8427–8456. https://doi.org/10.1029/2019ja027037

Sitnov, M. I., Stephens, G. K., Tsyganenko, N. A., Ukhorskiy, A. Y., Wing, S., Korth, H., & Anderson, B. J. (2017). Spatial structure and asymmetries of magnetospheric currents inferred from high-resolution empirical geomagnetic field models. In *Dawn-dusk asymmetries in planetary plasma environments* (pp. 199–212). American Geophysical Union (AGU). https://doi.org/10.1002/9781119216346.ch15

Sitnov, M. I., Tsyganenko, N. A., Ukhorskiy, A. Y., & Brandt, P. C. (2008). Dynamical data-based modeling of the storm-time geomagnetic field with enhanced spatial resolution. *Journal of Geophysical Research*, *113*(A7). https://doi.org/10.1029/2007JA013003

Sorathia, K. A., Merkin, V. G., Panov, E. V., Zhang, B., Lyon, J. G., Garretson, J., et al. (2020). Ballooning-interchange instability in the near-earth plasma sheet and auroral beads: Global magnetospheric modeling at the limit of the MHD approximation. *Geophysical Research Letters*, *47*(14), e2020GL088227. https://doi.org/10.1029/2020gl088227

Sorathia, K. A., Michael, A., Merkin, V. G., Ohtani, S., Keesee, A. M., Sciola, A., et al. (2023). Multiscale magnetosphere-ionosphere coupling during stormtime: A case study of the dawnside current wedge. *Journal of Geophysical Research: Space Physics*, *128*(11), e2023JA031594. https://doi.org/10.1029/2023ja031594

Speiser, T. W. (1965). Particle trajectories in model current sheets: 1. analytical solutions. *Journal of Geophysical Research (1896-1977)*, *70*(17), 4219–4226. https://doi.org/10.1029/JZ070i017p04219

Stephens, G. K., Bingham, S. T., Sitnov, M. I., Gkioulidou, M., Merkin, V. G., Korth, H., et al. (2020). Storm time plasma pressure inferred from multimission measurements and its validation using van Allen Probes particle data. *Space Weather*, *18*(12), e2020SW002583. https://doi.org/10.1029/2020SW002583

Stephens, G. K., & Sitnov, M. I. (2021). Concurrent empirical magnetic reconstruction of storm and substorm spatial scales using data mining and virtual spacecraft. *Frontiers in Physics*, *9*, 210. https://doi.org/10.3389/fphy.2021.653111

Stephens, G. K., Sitnov, M. I., Korth, H., Tsyganenko, N. A., Ohtani, S., Gkioulidou, M., & Ukhorskiy, A. Y. (2019). Global empirical picture of magnetospheric substorms inferred from multimission magnetometer data. *Journal of Geophysical Research: Space Physics*, *124*(2), 1085–1110. https://doi.org/10.1029/2018JA025843

Stephens, G. K., Sitnov, M. I., Ukhorskiy, A. Y., Roelof, E. C., Tsyganenko, N. A., & Le, G. (2016). Empirical modeling of the storm time innermost magnetosphere using Van Allen Probes and THEMIS data: Eastward and banana currents. *Journal of Geophysical Research: Space Physics*, *121*(1), 157–170. Portico. https://doi.org/10.1002/2015ja021700

Stephens, G. K., Sitnov, M. I., Weigel, R. S., Turner, D. L., Tsyganenko, N. A., Rogers, A. J., et al. (2023). Global structure of magnetotail reconnection revealed by mining space magnetometer data. *Journal of Geophysical Research: Space Physics*, *128*(2), e2022JA031066. https://doi.org/10.1029/2022JA031066

Stephens, G. K., Weigel, R., Sitnov, M. I., & Tsyganenko, N. A. (2025). Reconstructing magnetotail reconnection events using data mining is feasible and repeatable [Dataset]. *Zenodo*. https://doi.org/10.5281/zenodo.17770432

Stern, D. P. (1979). The role of o-type neutral lines in magnetic merging during substorms and solar flares. *Journal of Geophysical Research*, *84*(A1), 63–71. https://doi.org/10.1029/ja084ia01p00063

Stern, D. P. (1987). Tail modeling in a stretched magnetosphere: 1. methods and transformations. *Journal of Geophysical Research*, *92*(A5), 4437–4448. https://doi.org/10.1029/JA092iA05p04437

Tashman, L. J. (2000). Out-of-sample tests of forecasting accuracy: An analysis and review. *International Journal of Forecasting*, *16*(4), 437–450. https://doi.org/10.1016/s0169-2070(00)00065-0

Torbert, R. B., Russell, C. T., Magnes, W., Ergun, R. E., Lindqvist, P.-A., LeContel, O., et al. (2016). The fields instrument suite on mms: Scientific objectives, measurements, and data products. *Space Science Reviews*, *199*(1–4), 105–135. https://doi.org/10.1007/s11214-014-0109-8

Trattner, K. J., Mulcock, J. S., Petrinec, S. M., & Fuselier, S. A. (2007). Location of the reconnection line at the magnetopause during southward imf conditions. *Geophysical Research Letters*, *34*(3). https://doi.org/10.1029/2006gl028397

Trattner, K. J., Petrinec, S. M., & Fuselier, S. A. (2021). The location of magnetic reconnection at earth's magnetopause. *Space Science Reviews*, *217*(3), 41. https://doi.org/10.1007/s11214-021-00817-8

Trattner, K. J., Petrinec, S. M., Fuselier, S. A., & Phan, T. D. (2012). The location of reconnection at the magnetopause: Testing the maximum magnetic shear model with themis observations. *Journal of Geophysical Research*, *117*(A1). https://doi.org/10.1029/2011ja016959

Tsyganenko, N. A. (1989). A magnetospheric magnetic field model with a warped tail current sheet. *Planetary and Space Science*, *37*(1), 5–20. https://doi.org/10.1016/0032-0633(89)90066-4

Tsyganenko, N. A. (1995). Modeling the earth's magnetospheric magnetic field confined within a realistic magnetopause. *Journal of Geophysical Research*, *100*(A4), 5599–5612. https://doi.org/10.1029/94JA03193

Tsyganenko, N. A. (1996). Effects of the solar wind conditions on the global magnetospheric configurations as deduced from data-based field models. In *Proceedings of the third international conference on substorms (ICS-3)* (pp. 181–185).

Tsyganenko, N. A. (1998). Modeling of twisted/warped magnetospheric configurations using the general deformation method. *Journal of Geophysical Research*, *103*(A10), 23551–23563. https://doi.org/10.1029/98JA02292

Tsyganenko, N. A. (2002a). A model of the near magnetosphere with a dawn-dusk asymmetry 1. mathematical structure. *Journal of Geophysical Research*, *107*(A8), SMP12-1–SMP12-15. https://doi.org/10.1029/2001JA000219

Tsyganenko, N. A. (2002b). A model of the near magnetosphere with a dawn-dusk asymmetry 2. parameterization and fitting to observations. *Journal of Geophysical Research*, *107*(A8), SMP10-1–SMP10-17. https://doi.org/10.1029/2001JA000220

Tsyganenko, N. A. (2013). Data-based modelling of the earth's dynamic magnetosphere: A review. *Annales Geophysicae*, *31*(10), 1745–1772. https://doi.org/10.5194/angeo-31-1745-2013

Tsyganenko, N. A. (2014). Data-based modeling of the geomagnetosphere with an imf-dependent magnetopause. *Journal of Geophysical Research: Space Physics*, *119*(1), 335–354. https://doi.org/10.1002/2013JA019346

Tsyganenko, N. A., Andreeva, V., Kubyshkina, M., Sitnov, M. I., & Stephens, G. K. (2021). Data-based modeling of the earth's magnetic field. In *Magnetospheres in the solar system* (pp. 617–635). American Geophysical Union (AGU). https://doi.org/10.1002/9781119815624.ch39

Tsyganenko, N. A., & Andreeva, V. A. (2014). On the "bowl-shaped" deformation of planetary equatorial current sheets. *Geophysical Research Letters*, *41*(4), 1079–1084. https://doi.org/10.1002/2014GL059295

Tsyganenko, N. A., & Andreeva, V. A. (2015). A forecasting model of the magnetosphere driven by an optimal solar wind coupling function. *Journal of Geophysical Research: Space Physics*, *120*(10), 8401–8425. https://doi.org/10.1002/2015ja021641

Tsyganenko, N. A., Andreeva, V. A., & Gordeev, E. I. (2015). Internally and externally induced deformations of the magnetospheric equatorial current as inferred from spacecraft data. *Annales Geophysicae*, *33*(1), 1–11. https://doi.org/10.5194/angeo-33-1-2015

Tsyganenko, N. A., Andreeva, V. A., Sitnov, M. I., Stephens, G. K., Gjerloev, J. W., Chu, X., & Troshichev, O. A. (2021). Reconstructing substorms via historical data mining: Is it really feasible? *Journal of Geophysical Research: Space Physics*, *126*(10), e2021JA029604. https://doi.org/10.1029/2021ja029604

Tsyganenko, N. A., & Fairfield, D. H. (2004). Global shape of the magnetotail current sheet as derived from geotail and polar data. *Journal of Geophysical Research*, *109*(A3). https://doi.org/10.1029/2003ja010062

Tsyganenko, N. A., & Peredo, M. (1994). Analytical models of the magnetic field of disk-shaped current sheets. *Journal of Geophysical Research*, *99*(A1), 199–205. https://doi.org/10.1029/93JA02768

Tsyganenko, N. A., & Sitnov, M. I. (2005). Modeling the dynamics of the inner magnetosphere during strong geomagnetic storms. *Journal of Geophysical Research*, *110*(A3). https://doi.org/10.1029/2004JA010798

Tsyganenko, N. A., & Sitnov, M. I. (2007). Magnetospheric configurations from a high-resolution data-based magnetic field model. *Journal of Geophysical Research*, *112*(A6). https://doi.org/10.1029/2007JA012260

Turner, D. L., Cohen, I. J., Bingham, S. T., Stephens, G. K., Sitnov, M. I., Mauk, B. H., et al. (2021). Characteristics of energetic electrons near active magnetotail reconnection sites: Tracers of a complex magnetic topology and evidence of localized acceleration. *Geophysical Research Letters*, *48*(2), e2020GL090089. https://doi.org/10.1029/2020gl090089

Ueno, G., Machida, S., Mukai, T., Saito, Y., & Nishida, A. (1999). Distribution of x-type magnetic neutral lines in the magnetotail with geotail observations. *Geophysical Research Letters*, *26*(22), 3341–3344. https://doi.org/10.1029/1999gl010714

Vassiliadis, D. (2006). Systems theory for geospace plasma dynamics. *Reviews of Geophysics*, *44*(2). https://doi.org/10.1029/2004RG000161

Wang, C.-P., Lyons, L. R., Nagai, T., & Samson, J. C. (2004). Midnight radial profiles of the quiet and growth-phase plasma sheet: The geotail observations. *Journal of Geophysical Research*, *109*(A12). https://doi.org/10.1029/2004JA010590

Wang, G. Q., Zhang, T. L., Wu, M. Y., Schmid, D., Cao, J. B., & Volwerk, M. (2019). Solar wind directional change triggering flapping motions of the current sheet: Mms observations. *Geophysical Research Letters*, *46*(1), 64–70. https://doi.org/10.1029/2018gl080023

Waters, C. L., Eastwood, J. P., Fargette, N., Newman, D. L., Goldman, M. V., Archer, M. O., et al. (2025). Bridging in situ satellite measurements and simulations of magnetic reconnection using recurrent neural networks. *Journal of Geophysical Research: Space Physics*, *130*(10), e2025JA034383. https://doi.org/10.1029/2025ja034383

Wei, Y. Y., Huang, S. Y., Rong, Z. J., Yuan, Z. G., Jiang, K., Deng, X. H., et al. (2019). Observations of short-period current sheet flapping events in the Earth's magnetotail. *The Astrophysical Journal Letters*, *874*(2), L18. https://doi.org/10.3847/2041-8213/ab0f28

Wettschereck, D., Aha, D. W., & Mohri, T. (1997). A review and empirical evaluation of feature weighting methods for a class of lazy learning algorithms. *Artificial Intelligence Review*, *11*(1), 273–314. https://doi.org/10.1023/A:1006593614256

Xiao, S., Zhang, T., Ge, Y., Wang, G., Baumjohann, W., & Nakamura, R. (2016). A statistical study on the shape and position of the magnetotail neutral sheet. *Annales Geophysicae*, *34*(2), 303–311. https://doi.org/10.5194/angeo-34-303-2016

Zhang, T. L., Baumjohann, W., Nakamura, R., Balogh, A., & Glassmeier, K. (2002). A wavy twisted neutral sheet observed by cluster. *Geophysical Research Letters*, *29*(19). https://doi.org/10.1029/2002gl015544